Title
Terahertz Polarimetric Imaging

Author
Kim, Dongjin

Publication Date
2020

Peer reviewed|Thesis/dissertation

UNIVERSITY OF CALIFORNIA

Los Angeles

Terahertz Polarimetric Imaging

A thesis submitted in partial satisfaction

of the requirements for the degree

Master of Science in Electrical and Computer Engineering

by

Dongjin Kim

2020

ABSTRACT OF THE THESIS

Terahertz Polarimetric Imaging

by

Dongjin Kim
Master of Science in Electrical and Computer Engineering
University of California, Los Angeles, 2020
Professor Benjamin S. Williams, Chair

Imaging in the terahertz (THz) regime (0.1-10 THz) has shown grown interest over the past couple decades. While the THz imaging field is maturing, little work has been done imaging at these frequencies using polarization as a contrast mechanism. The polarization state of light as it interacts with different media contains additional information such as surface features, birefringence, and diattentuation. In this thesis, a polarization sensitive THz single-pixel imaging system is demonstrated using a recently developed THz quantum-cascade external cavity surface emitting laser (QC-VECSEL). The QC-VECSEL provides a high power THz laser output with good beam quality, features that are ideal for single-pixel imaging. The polarization sensitive images are acquired by using a fast rotating polarizer as an analyzer. This modulates the polarization state of the image, allowing for lock-in detection. Additionally, comparisons between past imaging systems are made to spotlight specific improvements achieved in this work.

The thesis of Dongjin Kim is approved.

Achuta Kadambi

Mona Jarrahi

Benjamin S. Williams, Committee Chair

University of California, Los Angeles

2020

TABLE OF CONTENTS

LIST OF FIGURES

LIST OF TABLES

ACKNOWLEDGMENTS

I would like to thank my advisor, Professor Benjamin Williams, for his support and guidance throughout my research. I am grateful to work under his supervision and have learned a lot from him over the past few years. I would also like to thank my lab mates for their support and encouragement. I would especially like to thank Dr. Luyao Xu and Dr. Chris Curwen who helped fabricate and test the QC-VECSEL used in this work. I would also like to thank them for their generous counsel they provided me throughout the years. Many thanks to Jiawei Wang for his initial contributions to this imaging project. His work included building the original optical system for single-pixel imaging. Additionally, thanks to John Reno at Sandia National Laboratories for providing the MBE growth for the device used in this work. Lastly I would like to thank all my family and friends for supporting me throughout my studies.

VITA

2016–2018 B.S. in Electrical and Computer Engineering, University of California, Los Angeles (UCLA).

2018-present Graduate Student Researcher, Electrical and Computer Engineering, University of California, Los Angeles (UCLA).

CHAPTER 1

Introduction

The terahertz (THz) frequency band, loosely defined as the range 0.1-10 THz, is one of the least developed regimes in the electromagnetic spectrum. Often denoted as the "THz gap" (as shown in Fig 1.1), these frequencies fall right in between microwaves and the mid-infrared. This gap is a consequence of neither traditional electronics nor photonics methods being well-suited for the THz band. Thus, this area has been an exciting area of research over the past several decades, calling for newer methods and technologies specifically designed for these frequencies. One particular area that has shown grown interest over the past couple decades is THz imaging. The prospects of imaging in this frequency range have been known since the 1970s; but, the lack of feasible THz sources and detectors had made such experiments difficult [8].

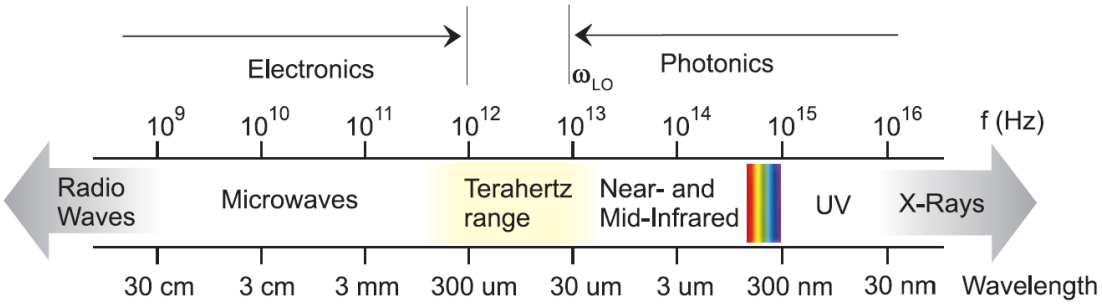

Figure 1.1: Diagram of the electromagnetic spectrum featuring the terahertz gap. Reproduced from [1]

However, the more recent growth of THz technologies, such as THz time-domain spectroscopy and novel THz sources, galvanized the field of THz imaging [9, 10]. In this chapter,

we will explore the applications of THz imaging, the technologies that make them possible, and the recent strides made in THz polarimetric sensing. While the THz imaging field is growing, relatively little work has been done imaging in this band using polarization information for added contrast. It is well known that polarization can provide complementary information to traditional intensity-based images since it has been studied in other regions of the electromagnetic spectrum such as the visible and infrared [11]. The polarization state of light as it interacts with various media can be altered, thus containing important properties regarding the media such as surface features, birefringence, and diattenuation [12, 13, 5]. In this thesis, a prototype THz imaging system is demonstrated as a testbed for polarization sensitive imaging.

1.1 Terahertz sources and detectors for imaging

While we cannot cover an exhaustive list of THz sources and detectors, we can highlight a few that have been spotlighted in the area of THz imaging. By far, the majority of THz imaging literature involves the use of THz time-domain spectroscopy (TDS) [9, 14]. It is a technique enabled by the emergence of ultrafast optoelectronics. In a typical THz TDS setup, a femtosecond laser pulse generates an ultrafast THz pulse through an emitter. After transmission or reflection from a sample, the resultant radiation is measured via photoconductive detection or electro-optic sampling, using the femtosecond laser as a probe pulse. By controlling a delay stage between the THz pulse and the femtosecond laser pulse, the time-domain electric field of the desired THz signal can be mapped out. Once this method was first demonstrated in the late 1980s, techniques to increase the data acquisition rate were readily established to make it viable for imaging [14].

A notable THz source that ushered in another wave of activity for THz imaging is the THz quantum-cascade laser (QCL). The QCL has the advantage of being compact while still being able to output tens of milliwatts of continuous wave power and watt level peak power [15, 16]. The QCL is based on intersubband transitions of electrons in a cascaded multiple

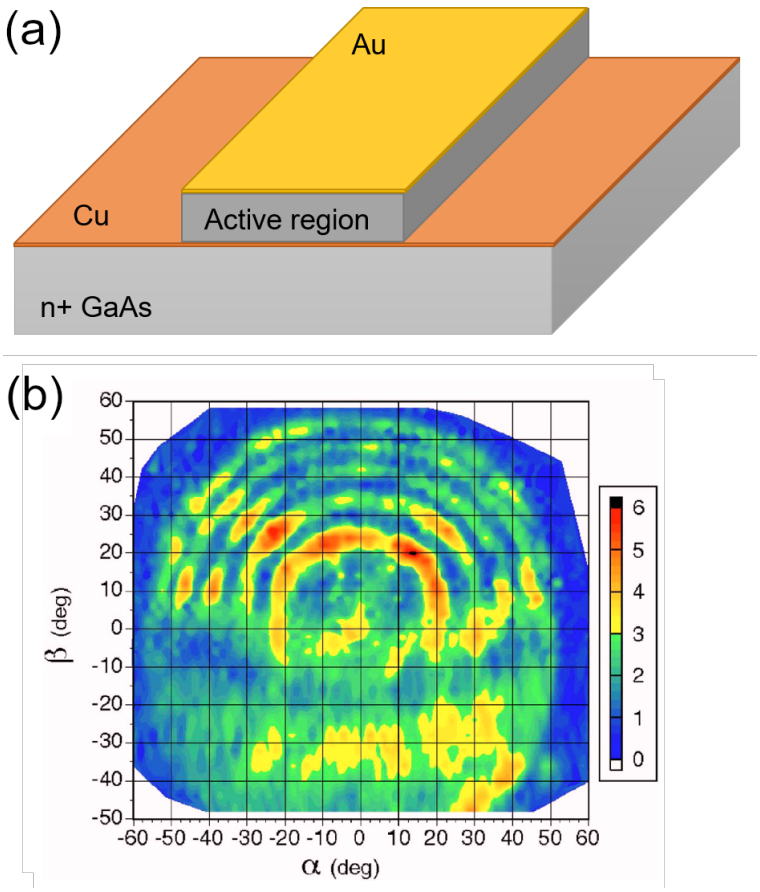

Figure 1.2: (a) Illustration of a metal-metal waveguide THz QCL. (b) Typical beam pattern of the design from (a). The subwavelength dimensions leads to a diffractive beam pattern [2].

quantum well heterostructure to provide gain. THz QCLs have generally employed two main architectures for cavity design: the metal-metal (MM) waveguide, and the surface-plasmon (SP) waveguide. The metal-metal waveguide has a very tight mode confinement due to the gain medium being sandwiched by two metal layers as shown in Fig 1.2(a). This reduces loss and allows this architecture to achieve higher power than its SP counterpart. However, due to the subwavelength dimensions of the cavity, the laser produces a highly diffractive beam pattern (see Fig 1.2(b)). On the other hand, SP waveguides have looser mode confinement due to the absence of a metal layer below the gain medium. These tend to have better beam patterns, but are more difficult to operate in continuous wave (CW). While these devices

typically operate at cryogenic temperatures, recent strides have brought up record operating temperatures up to 210 K [17]. Thus, it is no surprise that this technology has become a promising candidate for THz imaging in areas such as nondestructive evaluations, biomedical diagnostics, and even real-time imaging using a microbolometer focal-plane array [18, 19, 20].

1.2 The THz QC-VECSEL

The THz quantum-cascade vertical-external-cavity surface-emitting laser (QC-VECSEL) was first demonstrated in Professor Benjamin Williams' lab at UCLA in 2015 [21]. The QC-VECSEL design allows for high power output in addition to a good beam quality, alleviating the particular trade-offs between the MM and SP waveguide designs for typical QCLs. The design is based on an active reflectarray metasurface as shown in Fig 1.3. The metasurface is composed of subwavelength metal-metal ridges that couple in normally incident light at the TM_{01} waveguide mode. This patch antenna-like architecture is necessary to obey the intersubband polarization selection rule that necessitates electric fields to be parallel to the growth direction. The details of the theory are found in Ref [22]. A much improved beam quality is achieved because the laser effectively lases at a mode of the external cavity, which can be near-Gaussian.

For these reasons, the THz QC-VECSEL is an ideal candidate for single-pixel THz imaging, and is the illumination source used for this work. Fig 1.3, reproduced from Ref [3], shows an SEM image and a rough schematic of device. The dashed red circle in the SEM indicates the region in which current is injected; everywhere outside the circle has a layer of oxide underneath. This allows control over the effective bias area and also supports excitation of the fundamental Gaussian mode in the external cavity. In the context of the external cavity as shown in Fig 1.3(b), the metasurface acts as an amplifying mirror. The device shown in this figure has an additional implementation of a focusing effect. The external cavity is inherently a plano-plano cavity, which can have substantial cavity losses, increasing the laser threshold and lowering the maximum power output. To combat this, the ridge widths of the

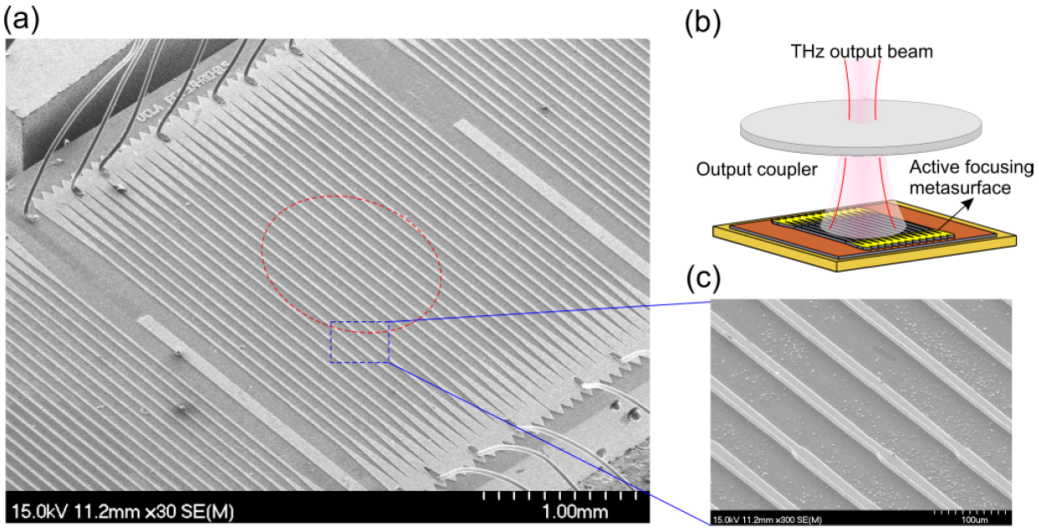

Figure 1.3: (a) SEM image of a THz QC-VECSEL. The metasurface is an array of subwavelength antennas loaded with QC gain material. The dashed red circle indicates the bias area. (b) Illustration of the device architecture. The metasurface acts as an amplifying mirror in an external cavity. (c) This particular device implements a focusing design in which the parabolic phase profile is embedded in the metasurface by radially varying the ridge width. This figure is reproduced from [3].

antennas are radially varied to match a parabolic phase profile to achieve a focusing mirror effect in addition to providing amplification. This design is implemented in the device used for this work.

1.3 Progress in THz polarimetric sensing

Since the initial excitement in the early 2000s, there have been countless ventures into many different disciplines to survey the potential of THz imaging. Many of these applications involve systems based on THz-TDS. For instance, thickness monitoring of coatings in pharmaceuticals [23] or paint in the automotive industry [24] both benefit from the nondestructive properties of the THz frequency. Other examples include biomedical and clinical applications [19] that take advantage of the frequency's strong sensitivity to water molecules. Several re-

cent publications have already well surveyed the advancements in THz imaging over the past few decades [10, 25, 26]. However, polarization sensitive THz imaging and sensing has yet to see much spotlight. In this section, we take a closer look at the progress in THz polarimetric imaging to ultimately motivate the imaging demonstrated in this work.

One of the first demonstrations of THz polarimetric imaging was by Van der Valk *et al.* in 2005 [4]. In this work, an electro-optic sampling scheme is constructed for measuring the polarization state of a THz pulse transmitted through a sample. A schematic of the setup is shown in Fig 1.4(a). The THz beam formed by a photoconductive emitter is focused by an off-axis parabolic (OAP) mirror onto a (111)-oriented ZnTe detector crystal. A circularly polarized optical probe pulse is focused onto the crystal, where the electric field of the THz beam is encoded onto the probe pulse. Finally, it passes through a half-wave plate followed by a Wollaston prism for differential detection. The half-wave plate allows for easy control over which electric-field component is measured relative to the crystal axes as illustrated by the inset in Fig 1.4(a). A plastic coin was raster scanned and the resultant power in two orthogonal polarization directions were measured. The two images on the left in Fig 1.4(b) show the parallel ($E_{\perp}$) and perpendicular ($E_{\parallel}$) components. The top right figure shows a photo of the sample for reference. The image on the bottom right is an image constructed from the relative angle of polarization, $\tan^{-1}\left(\frac{E_{\perp}}{E_{\parallel}}\right)$. A key feature in this image are the dark regions corresponding to large rotations in the polarization angle up to 45°. This provides evidence that the regions of contrast in the intensity based images are a result of reflection and scattering, rather than absorption in the material; an traditional intensity based image alone would not be able to distinguish between those different causes. Similar works, such as that in Ref [27], were published soon after in efforts to improve the signal strength and further analyze the obtained polarization sensitive images. More recently, this technique was implemented with a rotating electro-optic crystal to perform so-called time-domain polarimetry (THz-TDP) to obtain sensitivities up to 0.5° in determining polarization angles [28]. This was assisted by making post-measurement calibrations using Jones formalism to model systematic errors in the polarization state.

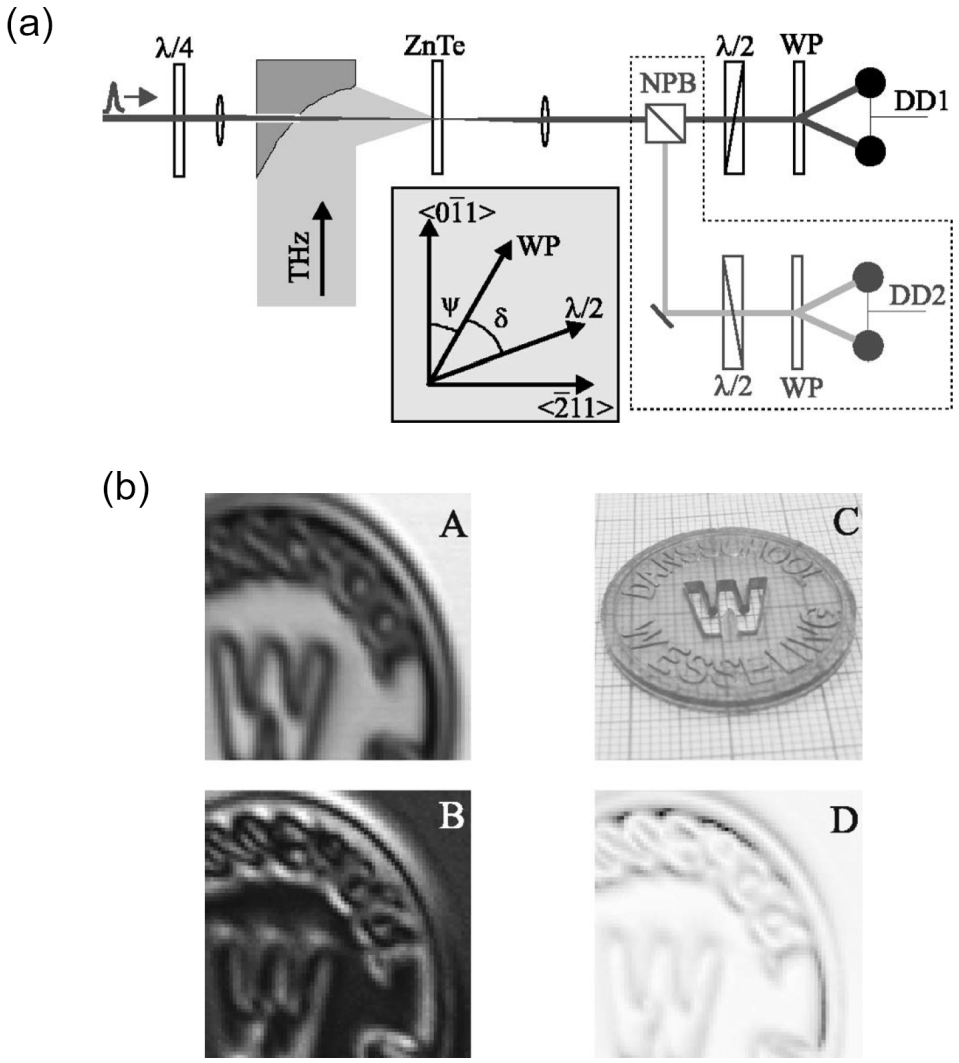

Figure 1.4: (a) Schematic of electro-optic polarization sensitive THz imaging system. (b) The two images on the left are measurements of the parallel and perpendicular components of the electric field. The top right image is a photo of the imaged sample — a plastic coin. The bottom right image shows the relative angle of polarization covering a range of 45°. The figure is reproduced from [4].

Because this topic of research is relatively immature, there has been a drive to explore novel applications where THz polarimetric sensing can serve as a unique tool. For instance, Sakai *et al.* recently demonstrated THz polarization sensitive imaging on *m*-plane GaN surfaces for identifying defects [29]; such diagnostics could be useful in improving GaN based

technologies such as high power transistors. Using laser THz emission microscopy (LTEM), a femtosecond laser induces THz radiation from the surface due to induced photocurrent. This probes the distribution of polar states across the surface and can identify regions with strong built-in electric fields. A wire-grid polarizer placed before detection of the THz pulse acts as an analyzer and allows separate detection of orthogonal surface polarization directions on the GaN surface. This technique demonstrated a unique advantage over traditional methods, like photoluminescence, since those techniques could not provide any information about local polar states and non-radiative defects.

Another instance of THz polarization sensitive sensing being used is in fundamental physics research. Jenkins *et al.* in 2010 demonstrated measurements of circular dichroism and Faraday rotation of THz frequencies under magnetic fields to study the optical Hall effect [5]. In fact, the imaging system in this thesis got its inspiration from this work. The setup used is shown in Fig 1.5(a). A THz molecular gas laser is steered onto a linear polarizer followed by a mechanically rotating waveplate. The rotator modulates the polarization state of the THz beam which is then sent into a sample with a controlled temperature and magnetic field. The final signal is measured by a lock-in amplifier with a reference signal from the mechanical rotator, allowing for extraction of particular Fourier coefficients of the modulated THz signal. By modeling the polarization state of the THz beam after the sample, the induced Faraday rotation can be written as a function of the DC, 2ω, and 4ω components of the THz beam, where ω is the angular frequency of the rotating waveplate. A doped single crystal Bi-2212 sample was measured under a magnetic field swept from -8 T to 8 T (see Fig 1.5(b)). The real and imaginary components of the Faraday angle characterize to the induced polarization rotation and ellipticity respectively. The results show an impressive sensitivity of 20 μrad/T, assisted by robust sample mounting and He-cooled Si bolometers.

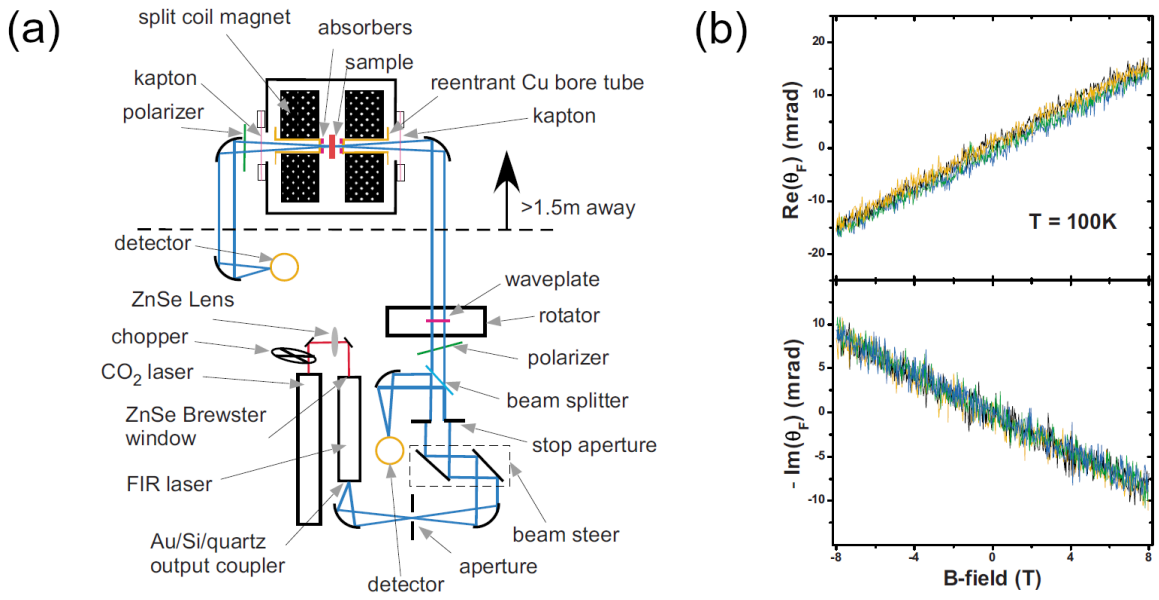

Figure 1.5: (a) Schematic of the optical system for measuring the complex Faraday angle of a THz beam induced by an applied static magnetic field. (b) The real and imaginary components of the Faraday angle for a doped single crystal Bi-2212 sample at 100 K. These components correspond to the orientation angle and ellipticity of the polarization state respectively. The results demonstrate a sensitivity of 20 μrad/T for the induced Faraday rotation. The figure is reproduced from Ref [5].

1.4 Thesis overview

The goal of this thesis is to demonstrate a polarization sensitive THz imaging system using a QC-VECSEL as the illumination source. Chapter 2 shows the measured properties of the particular device in use such as its electrical characteristics and power output. Chapter 3 goes through the important formalism and mathematical theory involved in modeling the polarization state of light. Chapter 4 details the THz imaging system, its performance, and the results achieved. Because this project is inherited from a previous graduate student, this chapter will also highlight the particular improvements made to past systems in an effort to achieve better sensitivity and spatial resolution. Finally, Chapter 5 discusses the outcome of this work and comments on any future research to be conducted.

1.5 Thesis contributions

Listed are the major contributions made in this work.

- Demonstration of a polarization sensitive THz single-pixel imaging system with a measured noise equivalent rotation angle of 0.30 mrad/$\sqrt{\text{Hz}}$.
- Characterization of the performance of the QC-VECSEL architecture in a polarization sensitive THz single-pixel imaging in terms of power output, polarization purity, and spatial resolution.
- Demonstration of various methods to improve the signal-to-noise ratio and spatial resolution of the THz imaging system.

CHAPTER 2

Source characterization

A QC-VECSEL, as described in Chapter 1, is used as the illumination source of the single-pixel THz imaging system detailed in Chapter 4. In this chapter, I describe the mounting process and laser's key characteristics that are important in realizing the optical system. These include the electrical properties, power output, beam quality, and its polarization state.

2.1 Device mounting

The fabricated pieces are cleaved, and each device is indium soldered onto a copper chip carrier. Gold pads are soldered onto the same chip carrier for making contacts to the metasurface via wirebonding. The chip carrier is then attached to a larger copper heat sink to be fitted inside a cryostat for liquid nitrogen temperature operation (77 K). The external cavity is formed with an output coupler mounted above the metasurface as shown in Fig 2.1. The screws attaching the output coupler mount to the heatsink are encased by springs to allow for continuous adjustment of the cavity alignment via a kinematic mount. The cavity was aligned using a HeNe laser by aligning the specular reflections from the output coupler and the metasurface. The VECSEL is then mounted intracryostat with a polymethylpentene (TPX) output window. The TPX window has about 80% transmittance at the laser frequency 3.4 THz. The output coupler (OC) for the external cavity is a metal mesh deposited on a z-cut quartz substrate [30]. The dimensions of the metal mesh determine the transmittance of the OC, and ultimately affect the threshold current density of the device and its output power. The designed output couplers typically had a transmittance that ranged

from 1-20%. For imaging, a larger power output is sought to achieve a better signal-to-noise ratio (SNR). For this device, a thin substrate (100 μm) is used with to mitigate Fabry-Perot induced instabilities in the output power. The experimental data for this particular OC is not available, but it is based on a 20% transmittance design at 3.4 THz.

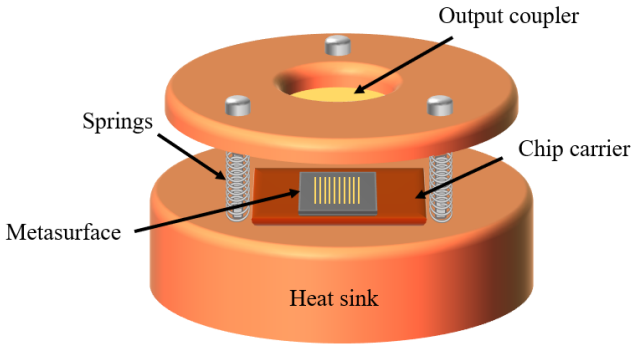

Figure 2.1: Illustration of the VECSEL after mounting for intracryostat operation. The springs allow for continuous tuning of the alignment between the metasurface and the output coupler.

2.2 TM_{01} focusing metasurface design

The metasurface was fabricated from a wafer grown in Sandia National Laboratories (labeled as VB0739) based on an active region design labeled as RPC163-M1 aimed at 3.3 THz. A focusing design was implemented as reported in Ref [3]. Because of the TM_{01} resonance characteristic of the metal-metal waveguide, a wide tuning range of the phase response of the metasurface can be achieved by varying the ridge widths. Then, by radially varying the ridge widths to form a parabolic phase profile, a focusing effect of a plane wave can be achieved; in this way, the metasurface also acts as a parabolic mirror. The purpose of this design is to minimize diffraction losses of the external cavity relative to a plano-plano configuration, lowering the laser threshold. This may also allow higher transmittance output couplers to be used depending on how much the focusing effect can compensate for the additional losses.

2.2.1 L-I-V and spectra measurement

The light-current-voltage (L-I-V) characteristics of the device at 77 K were measured in pulsed mode using a boxcar averager. Fig 2.2(a) illustrates the measurement setup. The boxcar reads the voltage and current (via a current sensor loop) through the device during each pulse and sends each signal to a digital multimeter (not shown in figure) for data acquisition. The boxcar's output is calibrated with a source meter to ensure that they are accurate to the true voltage and current values. A room-temperature operated pyroelectric detector with a black absorber (Gentec-EO QS5-THz-BL) is used to detect the power output. A pyroelectric detector only responds to slow varying AC signals, so the pulser (Avtech AVR-7B-B) is gated by a slow square wave (>5 Hz). This achieves the same effect as an optical chopper, but produces less noise. An illustration of the biasing scheme is shown in Fig 2.2(b) that allows for simultaneous light-current-voltage measurements. The repetition rate for the pulser will be labeled as f_{fast} and the frequency of the gate as f_{slow}. To measure the voltage signal from the detector, a lock-in amplifier (SRS SR830) is used with the gate signal as the reference frequency. The lock-in amplifier enables phase-sensitive detection for increased sensitivity.

The resultant L-I-V characteristics are shown in Fig 2.3. For these plots, the pulser was set at a repetition rate of 10 kHz (f_{fast}) with a 500 ns pulse width. As mentioned, the pulses were electrically gated with a square wave to simultaneously measure the light power output, resulting in an effective duty cycle of 0.25% for the laser bias. The maximum responsivity of the pyroelectric detector occurs at a chopping frequency (f_{slow}) of 5 Hz. However the gate was set to 100 Hz to remain under the maximum voltage limit of the lock-in amplifier input. To obtain the voltage responsivity of the pyroelectric detector, the power output was measured with a thermopile detector (Scientech AC2500). The thermopile measures average power, so the peak power can be calculated based on the duty cycle used. That is,

$$P_{peak} = P_{avg}(\text{DC})_{therm} \quad , \tag{2.1}$$

where $(\text{DC})_{therm}$ is the duty cycle used for the power measurement, 7.5%. The duty cycle

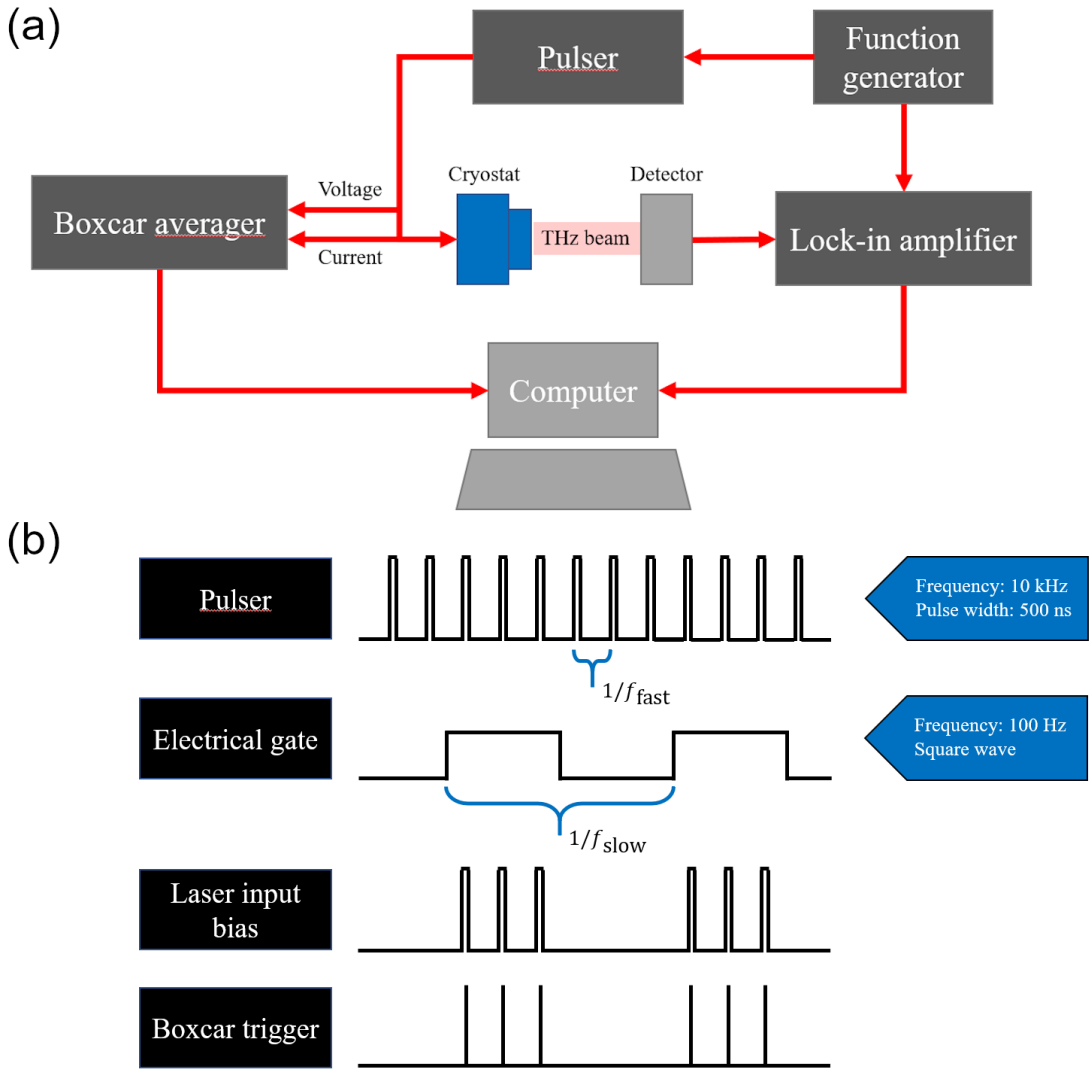

Figure 2.2: (a) Schematic of the measurement setup for measuring the LIV characteristics of intracryostat VECSEL. The detector is a $LiTaO_3$ pyroelectric detector operated at room temperature. The function generator provides the gate signal to chop the pulser and is fed into the lock-in amplifier as the reference signal. (b) An illustration of the laser biasing scheme. An electrical gate modulates the pulser with a slower varying square wave set at 100 Hz (f_{slow}) for this measurement. This chops the laser output so that it can be measured by a pyroelectric detector. The IV is simultaneously measured with the boxcar averager.

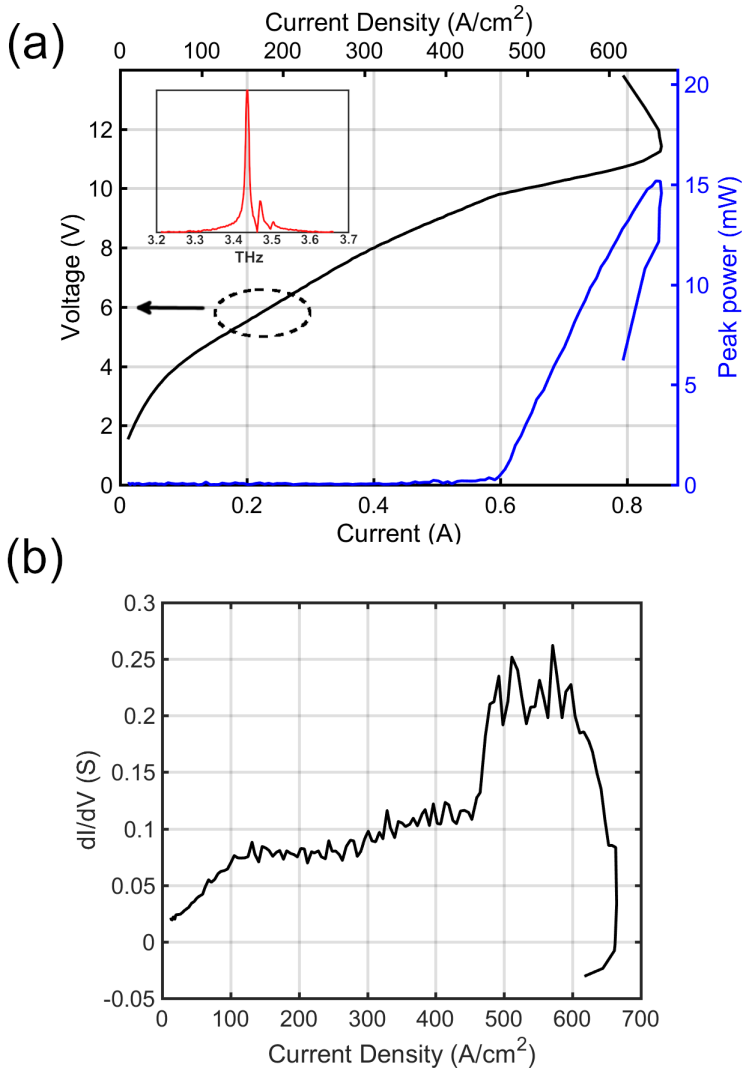

Figure 2.3: (a) The L-I-V plot of the QC-VECSEL at 77 K in pulsed mode (0.25% effective duty cycle). The pulser repetition rate is set at 100 kHz (f_{fast}) and a pulse width of 1 μs. The plot shows both the current and current density corresponding to an effective bias area of 0.00129 cm^2. The laser threshold occurs at 465 A/cm^2 and has a maximum current density of 660 A/cm^2. The maximum peak power of 15 mW is reached. Note that the power values here include the added attenuation from the TPX output window of the cryostat. The inset shows the lasing spectrum measured using an FTIR. (b) The measured dI/dV obtained from (a). The lasing threshold can be characterized by the jump in the dI/dV curve.

here is increased in order to increase the average power output for better signal-to-noise ratio from the thermopile output. This will introduce some error due to temperature degradation of the device as will be discussed later in this chapter. Then, the voltage responsivity is obtained from

$$R_v = \frac{V_{sig}}{P_{peak}(\mathrm{DC})_{IV}} \quad , \tag{2.2}$$

where V_{sig} is the measured lock-in output signal and $(\mathrm{DC})_{IV}$ is the duty cycle used for the L-I-V measurement, 0.25%. A responsivity of 2667 V/W is measured. The thermopile was calibrated against a Thomas Keating THz absolute power meter, the accuracy was determined to be about 5% at 3.4 THz. The recorded power values in Fig 2.3(a) do not take into account the collection efficiency of the measurements. However, to maximize the collection efficiency, the thermopile was positioned as close to the output window of the cryostat as possible. Additionally, the power measurements reflect the power that is actually detected, meaning that the attenuation from the TPX output window is included in the measurement. Both the current and the current density, J, are shown in the plot using the effective area of the biased region in the metasurface (0.00129 cm^2). Fig 2.3(a) shows that the laser threshold is around 465 $\mathrm{A/cm}^2$ and reaches a maximum current density of 660 $\mathrm{A/cm}^2$. The peak power output reaches a maximum of 15 mW before quickly dropping off as we enter the negative differential resistance regime. The lasing spectrum is measured with a Fourier-transform infrared spectrometer (FTIR) with a deuterated triglycine sulfate (DTGS) detector; the spectrum is showed in the inset of Fig 2.3(a). The laser primarily lases at 3.44 THz, but has smaller sidemodes at 3.47 and 3.5 THz. This suggests that the free spectral range (FSR) of the external cavity is 30 GHz corresponding to a cavity length of 5 mm, which roughly agrees with a physical estimate. Fig 2.3(b) shows the calculated dI/dV. The laser threshold is characterized with a discontinuity in the differential conductance of the device due to the onset of stimulated emission. This adds a new mechanism that reduces the upper state lifetime and thus increases the conductivity of the device.

2.2.2 Demonstrating device sensitivity to duty cycle

The temperature characteristics of this device can be demonstrated by tuning the duty cycle of pulsed operation. The L-I-V shown in Fig 2.3(a) was obtained with the pulser set at a 100 kHz (f_{fast}) repetition rate and 500 ns pulse width (0.5% duty cycle). This was purposely chosen to minimize the effects of heating during the measurement. As the temperature rises, the rate of LO-phonon scattering for electrons in the upper laser level increases. These nonradiative transitions quickly depopulate this subband, significantly decreasing the upper state lifetime. For the QC-VECSEL, these effects manifest themselves in increasing the lasing threshold and decreasing the peak power for a given current density [30]. A larger duty cycle will increase the average lattice temperature and thus heat up the electron gas, resulting in a reduction in power output. This effect is more dramatic with increasing pulse width, but is also apparent with increasing repetition rate (at a fixed pulse width). In an experiment, the light output of the QC-VECSEL versus the pump duty cycle is measured. The current density is kept constant ($\sim$660 A/cm^2) in addition to the pulse width (1 μs). Then, the repetition rate of the pulse train, f_{fast}, is varied from 5 kHz to 120 kHz. The gate frequency, f_{slow}, is kept constant at 200 Hz. If there was no temperature degradation, the peak power at a given current should remain independent of the duty cycle of the pulse train, and the average power would scale proportionally. However, as can be seen in Fig 2.4, the peak power decays with the duty cycle. Moreover, the signal detected no longer increases past a duty cycle of 11%. While it is desirable to maximize the average power output of the device for SNR purposes, one must be mindful of simply scaling up the duty cycle. Taking this into consideration, the device is operated at a pulser repetition rate of 100 kHz (f_{fast}) and 1 μs pulse width, resulting in a 10% duty cycle, for most of the imaging experiments.

2.2.3 Measuring beam quality factor

Another important attribute of the device that must be characterized is the beam quality. The beam pattern and its divergence are important aspects in many imaging modalities such

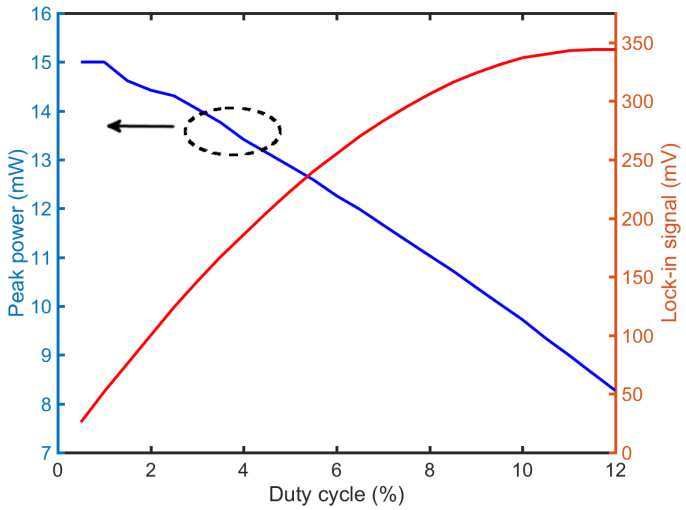

Figure 2.4: A plot demonstrating the light output versus the pump duty cycle. The red curve corresponding to the right axis is the measured signal from the pyroelectric detector. The blue curve corresponding to the left axis is the calculated peak power. The measurements were performed at the maximum current density, 660 A/cm^2, and a constant pulse width, 1 μs.

as single-pixel imaging. The QC-VECSEL has the advantage of obtaining near ideal TM_{00} Gaussian beam profiles — a significant improvement from a typical metal-metal ridge QCL — due to the external cavity supermode. While there are many ways to quantify the beam quality, the most universally accepted is the M^2 method [31]. The quantity M^2 can be best described as the ratio between the measured beam divergence and the beam divergence of an ideal Gaussian beam with the same beam waist. This quantity ($M^2 \geq 1$) then provides us with a metric that characterizes relatively how close the measured beam is to a diffraction-limited one. The underlying physics behind this method is based on establishing the beam width using second moments. The second moment of an arbitrary laser beam intensity profile rigorously follows a quadratic propagation equation [31]. By using the M^2 as a correction factor to the ideal Gaussian beam propagation equation, it is possible to model an arbitrary

laser beam using the same form. That is,

$$w'(z) = w'_0\sqrt{1 + \left(\frac{z - z_0}{z_R}\right)^2} \tag{2.3}$$

where $w'(z)$ is the beam radius at a given longitudinal location z, w'_0 is the beam waist, z_0 is the location of the beam waist, and z_R is the Rayleigh range. The primed values represent quantities that model the arbitrary laser beam. Then, a simple relationship between the real beam and an ideal beam can be summarized as follows:

$$w'_0 = Mw_0 \tag{2.4}$$

$$z_R = \frac{\pi(w'_0)^2}{M^2\lambda} \tag{2.5}$$

$$\theta' = \frac{2\lambda M^2}{\pi w'_0} \tag{2.6}$$

By setting the beam waist and location of the measured beam to be that of an ideal Gaussian beam, the relationship between the real and ideal divergence angles can be established:

$$M^2 = \frac{\theta'}{\theta} \tag{2.7}$$

The standards for accurately measuring M^2 values have been established by the International Organization for Standardization [32]. Because an arbitrary beam can have different types of asymmetry including astigmatism, it is important to sample enough points within and outside the Rayleigh range. Because of the extra degree of freedom in the M^2 factor, an arbitrary monochromatic beam can have infinite solutions for the beam divergence given a fixed beam waist. The converse is also true; infinite solutions for the beam waist exist given a fixed divergence angle. To measure the beam radii for the QC-VECSEL, a simple knife-edge technique is used. This technique has the advantage of achieving higher SNR compared to other methods like the slit or pinhole method. Since the initial beam waist is located near the output coupler of the device, this region is inaccessible. Therefore, the beam is first focused by a 1 in. diameter biconvex high-resistivity silicon lens (1 in. focal length) placed 3 inches

from the output coupler. Using the results from a separately measured radial beam pattern (see Fig 2.5(b)), the full width half maximum (FWHM) diameter of the beam incident on the lens is known to be about 6 mm, ensuring that the M^2 results are not affected by spatial filtering.

Using the focal length of the lens as a rough starting point, the beam radii are measured by stepping the knife-edge transverse to the optical axis. The beam is then refocused to be captured by a room-temperature pyroelectric detector. A step size of 0.1 mm for the knife-edge is used, allowing for enough sample points throughout the beam diameter. The beam spot size was measured at increments of 1 mm in the longitudinal direction, allowing for enough samples within and outside the Rayleigh range.

The transverse cuts of the beam intensity produced by the knife-edge measurement can be fitted to an error function, modeling the integration of the transverse profile. While there are many ways to define the beam width, the M^2 method abides by the second moment definition of beam width. To obtain an accurate second moment measurement of this cross-section, the pinhole method must be used. However, since our beam has no apparent side-lobes, a good approximation of the second moment beam diameter can still be made by calculating twice the distance between the 16% and 84% transmission locations of the knife-edge measurement [33]. This is because those thresholds correspond to the $1/e^2$ values of a Gaussian beam intensity (this is often called the D86 width). An example of a single cut measurement is shown in Fig 2.5(a). The data is fitted to an error function, which models the integrated light intensity profile in the transverse plane. Using the fit to extract the beam widths for every slice over several longitudinal positions, the beam diffraction can be plotted, as shown in 2.5(b). The data here is fitted to Eq 2.3 using the method of least squares. The data shows a good fit to the model ($R^2 \sim 99.5\%$), and predicts a beam waist of 0.325 mm. The Rayleigh range can be graphically identified since it indicates the position in which the beam radius has expanded by a factor of $\sqrt{2}$. Thus, using Eq 2.5, the M^2 value can be readily obtained:

$$M^2 = \frac{\pi(w_0')^2}{\lambda z_R} \tag{2.8}$$

In this measurement, we obtain $M^2 \approx 1.97$.

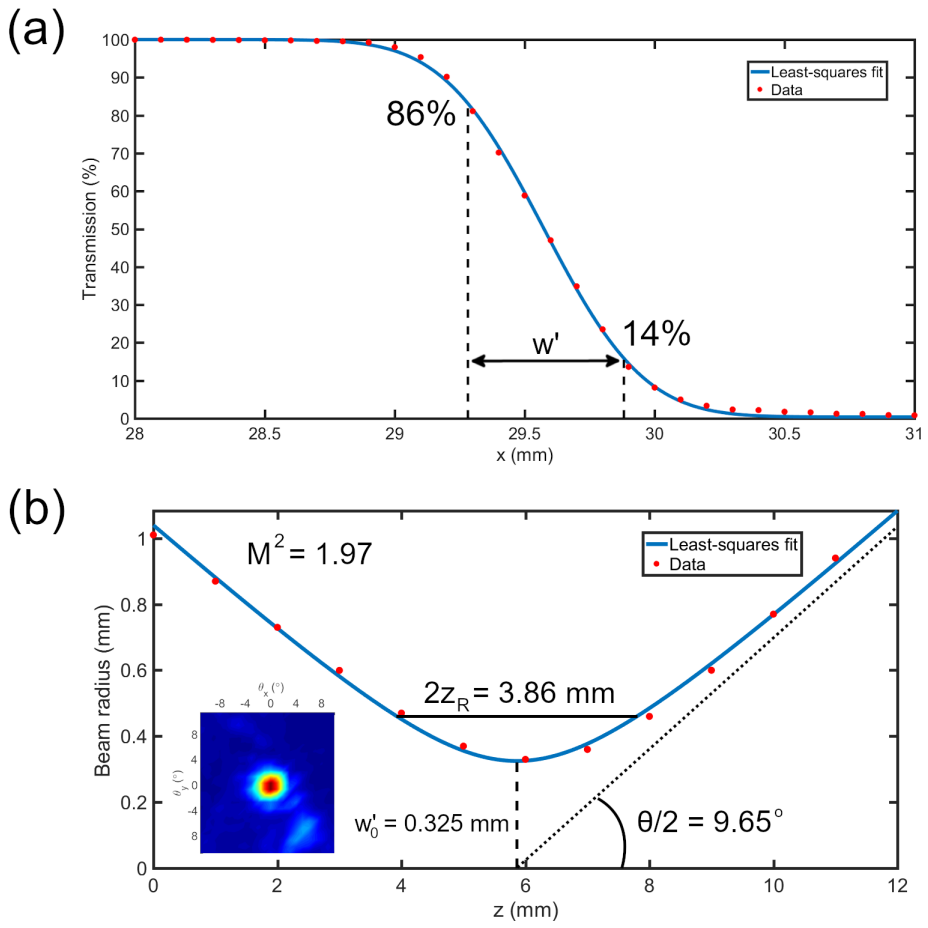

Figure 2.5: (a) A transverse cut of the QC-VECSEL beam measured by the knife-edge method. The data is fitted to an error function. The dashed lines represent the defined beam width for each measurement. (b) The beam divergence behavior is plotted using the measured beam widths at several longitudinal positions around the beam waist position. An M^2 value of 1.97 is calculated. The inset shows a separately measured beam pattern of the diverging beam from the laser output with a full-width half-maximum of $\sim 4° \times 4°$.

The knowledge of the M^2 value allows for easy calculation of the divergence behavior of the real beam in any optical system without abberations. For example, this result can be used to estimate the divergence of the beam from the output of the laser. The VECSEL has a beam waist roughly equal to the radius of the bias area, which for this device is 0.5 mm.

Then, for a wavelength of 87 μm, the angle of divergence assuming a Gaussian beam is 6.4°. Using the obtained M^2, the actual beam divergence must be closer to 12.6°. We can convert this value into a more familiar FWHM definition for the beam divergence. The Gaussian beam intensity profile is given by

$$\frac{I}{I_0(z)} = \exp\left(-2\left(\frac{r}{w(z)}\right)^2\right) \quad , \tag{2.9}$$

where $I_0(z)$ is the peak intensity for a given z coordinate. The divergence angle is

$$\theta = 2\frac{w(z)}{z} \quad , \tag{2.10}$$

and we define

$$\gamma = 2\frac{r}{z} \quad . \tag{2.11}$$

Then, we can write Eq 2.9 in terms of the divergence angle:

$$\frac{I}{I_0(z)} = exp\left(-2\left(\frac{\gamma}{\theta}\right)^2\right) \quad . \tag{2.12}$$

Setting this equal to half, γ will represent the FWHM divergence angle. That is,

$$\ln\frac{1}{2} = -2\frac{\theta_{FWHM}^2}{\theta^2} \quad , \tag{2.13}$$

resulting in

$$\theta_{FWHM} = \theta\sqrt{\frac{1}{2}\ln 2} \quad . \tag{2.14}$$

This estimates the FWHM divergence angle from the output of the laser to be 7.4° in the x direction. Comparing this to the measured beam pattern shown in the inset of Fig 2.5(b), the actual FWHM beam divergence is about 4° in both directions. The discrepancy in the estimated value is mostly due to the approximated beam waist in the VECSEL cavity, which was assumed to be equal to the bias circle. Thus, the estimated value can serve as a good upper bound for the laser beam divergence.

Nevertheless, it is important to consider the accuracy of the results obtained is this measurement. Sources of error include abberations due to the focusing lens, diffraction and reflections from the knife-edge, and the goodness of the fit. Having a small spot size incident

on the lens mitigates the effects of spherical abberations. Additionally, the latter of these three can be well characterized because of the known model. The ability to determine a unique fit to Eq 2.3 is sensitive to the longitudinal position of the measured samples. If we define a normalized longitudinal position given by

$$\zeta = \frac{z}{z_R} \ , \tag{2.15}$$

then the relative change in the true beam waist versus the closest sampled beam radius is given by

$$r = \sqrt{1 + (\zeta_0)^2} - 1 \ . \tag{2.16}$$

In other words, an upper bound for the longitudinal distance, ζ_0, between the position of the true beam waist and the closest measured position can be found for a given percent accuracy of the beam waist value:

$$\zeta_0 \leq \sqrt{(r+1)^2 - 1} \ . \tag{2.17}$$

To achieve an error of less than 10% for the beam waist, at least one of the sampled points

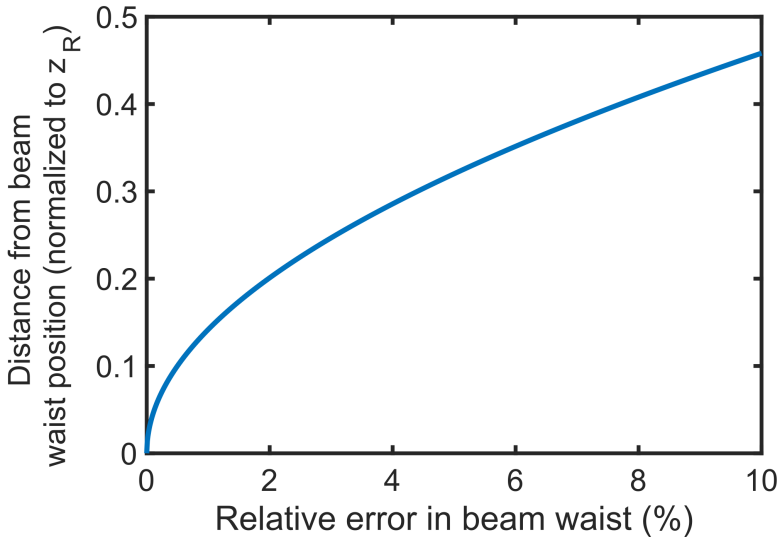

Figure 2.6: A graphical representation of Eq 2.17

must be within half a Rayleigh range from the true beam waist position. Fig 2.6 illustrates this on a plot. From the plot, it is clear that the accuracy of the beam waist falls very quickly

with ζ_0. This reinforces the importance of having enough samples within the Rayleigh range in M^2 measurements. The measurement described in Fig 2.5 used a longitudinal step size of 1 mm for a Rayleigh range of about 1.93 mm. This results in a maximum ζ_0 value of about 0.5. Based on this result, a rough upper bound for the error in the calculated beam waist is 10%. Indeed, more reliable measurements can be achieved with smaller increments in z. It is also possible to take non-uniformly spaced samples to more efficiently extract the M^2 value [33]. Furthermore, the measurements performed were only in one transverse plane. A more complete beam quality factor measurement would repeat the same steps in the orthogonal plane to obtain both $M_x{}^2$ and $M_y{}^2$ values. Nevertheless, a separately measured beam pattern of the device is shown in the inset of Fig 2.5(b) to illustrate the overall intensity profile.

2.2.4 Polarization properties

The QC-VECSEL has a near linearly polarized laser beam. A measurement conducted by previous graduate researcher, Jiawei Wang, is shown in Fig 2.7. A free-standing wire-grid polarizer (Microtech G30X10) was rotated by 180° as the transmitted light signal was measured by a pyroelectric detector; the measurements plot out a curve in accordance with Malus' Law. For the non-ideal case, Malus' Law can be written as

$$I_{out} = a_0(T_s + T_p) + a_1(T_s - T_p)cos(2\theta) \ , \tag{2.18}$$

where T_s and T_p represent the maximum and minimum transmittance of the wire-grid polarizer (WGP) respectively. The provided values for this WGP at 3 THz are $T_s = 0.965$ and $T_p = 0.014$. The axial ratio, defined as

$$AR = \left| \frac{a_0 + a_1}{a_0 - a_1} \right| \ , \tag{2.19}$$

quantifies the linear polarization purity. An ideal linearly polarized beam would have an axial ratio approaching infinity. Fig 2.7 shows a maximum intensity of 3 V and a minimum intensity of 0.0747 V. It is not necessary to convert these voltages to an intensity or AR measurements, since they are linearly related by the responsivity of the detector. Using these values along with Eq 2.18 and 2.19, an axial ratio of 20 dB is obtained. In other words, if an

ideal linear polarizer was used, the ratio between the maximum and minimum transmission would be 100. A high linear polarization purity will be advantageous in polarization sensitive imaging because it can bypass the need for an initial linear polarizer which would have its own insertion loss.

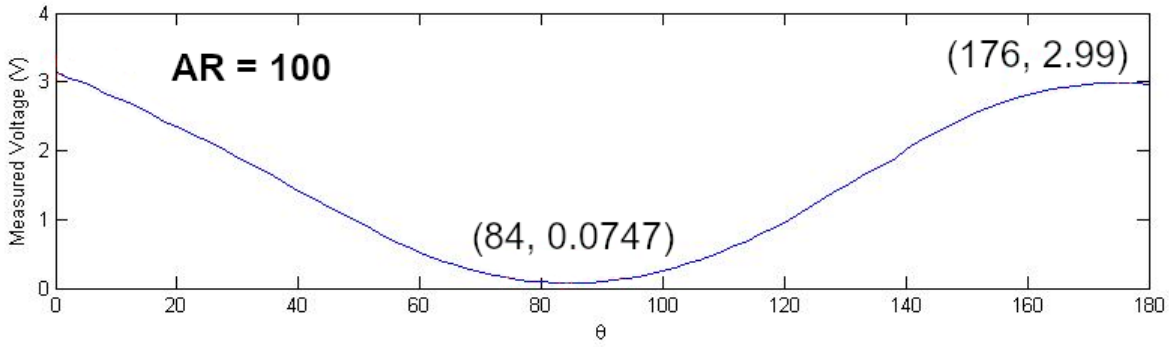

Figure 2.7: A free-standing wire-grid polarizer is rotated over 180° in front of the QC-VECSEL and measured via a pyroelectric detector. The two coordinates highlight the points of minimum and maximum transmission.

CHAPTER 3

Polarization Modeling

3.1 Jones calculus

3.1.1 The Jones vector

The plane wave solution to Maxwell's equations propagating in the z direction can be written as

$$\mathcal{E}(z,t) = (|E_{x,0}|e^{j\phi_x}\hat{\mathbf{x}} + |E_{y,0}|e^{j\phi_y}\hat{\mathbf{y}})e^{j(kz-\omega t)} \quad . \tag{3.1}$$

The terms inside the parenthesis contain information about the polarization state of the electromagnetic field. Each vector component has its own electric field amplitude and phase associated with it. What ultimately determines their polarization is the ratio of their amplitudes and the differences in their phase. To make this more explicit, we can rewrite Eq 3.1 as

$$\mathcal{E}(z,t) = E_0 e^{j\phi_x}(E_x\hat{\mathbf{x}} + E_y e^{j\delta}\hat{\mathbf{y}})e^{j(kz-\omega t)} \tag{3.2}$$

where

$$E_0 = \sqrt{|E_{x,0}|^2 + |E_{y,0}|^2} \tag{3.3}$$

$$E_x = \frac{|E_{x,0}|}{E_0} \tag{3.4}$$

$$E_y = \frac{|E_{y,0}|}{E_0} \tag{3.5}$$

$$\delta = \phi_y - \phi_x \quad . \tag{3.6}$$

In this way, the terms inside the parenthesis contain solely polarization information. Notice that the phase term in the x component can be factored out and disregarded in the analysis,

as it is just a global phase term in which its modification is equivalent to translating the illumination source in the propagation direction. Also note that Eq 3.2 is not well defined for $E_x = 0$, but is easily addressed by letting $\phi_x = \phi_y$. Then, to conveniently track the polarization state of the field in a given system, a vector can be formed:

$$\mathbf{E} = \begin{pmatrix} E_x \\ E_y e^{j\delta} \end{pmatrix} \quad . \tag{3.7}$$

This is called the Jones vector where the basis states are orthogonal linear polarization states (x and y). In general, the polarization state described by this vector is elliptical. The ellipse can be described by its orientation angle, ψ, and its ellipticity angle, χ, as shown in Fig 3.1. With a bit of Algebra, it can be shown that

$$\psi = \frac{1}{2} \tan^{-1} \left(\frac{2E_x E_y cos\delta}{E_x^2 - E_y^2} \right) \tag{3.8}$$

and

$$\chi = \tan^{-1} \left(\frac{E_{min}}{E_{max}} \right) \tag{3.9}$$

where either E_{min} or E_{max} is given by

$$E_{min} \text{ or } E_{max} = \sqrt{E_x^2 \cos^2 \psi + E_y^2 \sin^2 \psi + E_x E_y \cos\delta \sin 2\psi} \quad . \tag{3.10}$$

The complication arises from the fact that Eq 3.8 results in the angle that the major axis *or* the minor axis makes with the horizontal, depending on the specific values of the argument. This can be determined simply by evaluating Eq 3.10 at ψ and $(\psi + \frac{\pi}{2})$. However, in active polarimetric imaging, the polarization state of the illumination source is usually well known, making this less of an issue.

3.1.2 Jones matrices

With the Jones vector defined, any changes to the polarization state of light due to its interaction with materials, optical elements, or other environments, can be modeled by a multiplication with a corresponding transfer matrix. For instance, a linear polarizer with its

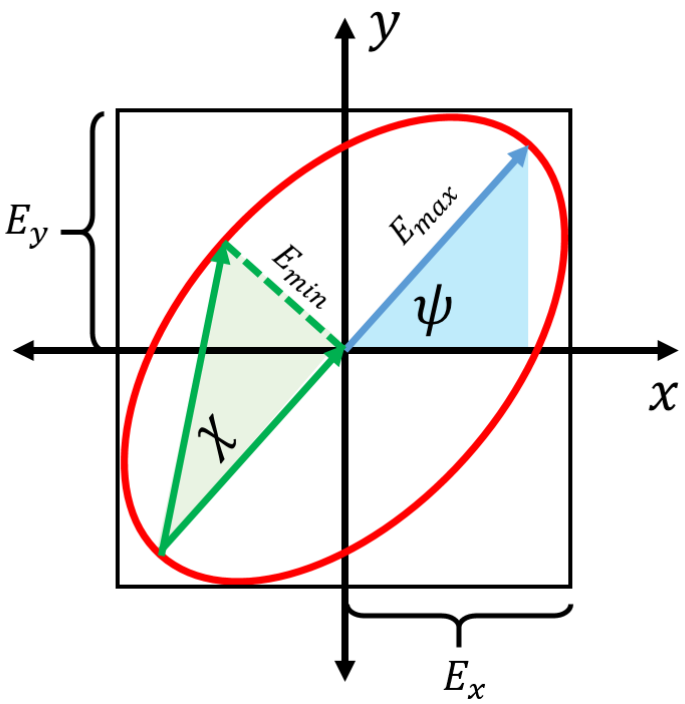

Figure 3.1: Projecting the time evolution of a propagating elliptically polarized plane wave on a fixed transverse plane (xy) creates an ellipse. The ellipse can be described by its orientation angle, ψ, and its ellipticity angle, χ. Although not illustrated here, an elliptical polarization is also distinguished by its chirality, or handedness, that depends on the phase difference between the orthogonal vector components.

transmission axis oriented along the x-axis is given by

$$\mathbf{J}_{HLP} = \begin{pmatrix} 1 & 0 \\ 0 & 0 \end{pmatrix} \quad . \tag{3.11}$$

These matrices can then be cascaded, accounting for any number of interactions, to output the final polarization state. That is,

$$\mathbf{E}_{out} = \mathbf{J}_N \cdots \mathbf{J}_2 \mathbf{J}_1 \mathbf{E}_{in} \quad , \tag{3.12}$$

where the indices of the Jones matrices indicate that each consecutive interaction is a matrix multiplication from the left. To obtain the Jones matrix for a linear polarizer oriented at an arbitrary angle, we can apply a rotation matrix as a transformation to the original matrix.

This results in

$$\mathbf{J}_{LP} = \mathbf{R}(-\theta)\mathbf{J}_{HLP}\mathbf{R}(\theta) \tag{3.13}$$

where

$$\mathbf{R}(\theta) = \begin{pmatrix} \cos\theta & -\sin\theta \\ \sin\theta & \cos\theta \end{pmatrix} \quad . \tag{3.14}$$

This leads to

$$\mathbf{J}_{LP} = \begin{pmatrix} \cos^2\theta & \sin\theta\cos\theta \\ \sin\theta\cos\theta & \sin^2\theta \end{pmatrix} \quad , \tag{3.15}$$

where θ is the angle of the transmission axis relative to the x-axis. A list of common Jones matrices is given in Table 3.1. In practice, one of the Jones matrices included in Eq 3.12 could be an arbitrary sample. In transmission mode, the sample's Jones matrix would simply be defined by its co-polarization and cross-polarization transmission components. We can write

$$\mathbf{J}_{sample} = \begin{pmatrix} t_{xx} & t_{xy} \\ t_{yx} & t_{yy} \end{pmatrix} \quad . \tag{3.16}$$

In general, these elements are complex-valued. In many cases, the sample may be rotationally invariant, resulting in a simplified model where $t_{xx} = t_{yy}$ and $t_{yx} = -t_{xy}$ [5]. Finally, what is actually measured is the intensity, which is obtained by taking the square of the magnitude of the final output Jones vector, $\mathbf{E}_{out}$, in Eq 3.12. Therefore, the optical elements are carefully chosen so that the elements in Eq 3.16 can be obtained from the intensity measurements of the final Jones vector. In general, all four elements cannot be obtained with a single measurement. A canonical system for polarization sensitive sensing is given by

$$\mathbf{E}_{out} = \mathbf{J}_{LP,2}\mathbf{J}_{sample}\mathbf{J}_{LP,1}\mathbf{E}_{in} \quad , \tag{3.17}$$

where the first linear polarizer is to create a well-known polarization state for the light going into the sample, and the second linear polarizer is the analyzer. This setup is analagous to a typical ellipsometry setup. The formalism established by this Jones calculus allows convenient modeling of the polarization state of light in any optical system. It has been used in conjunction with THz time-domain spectroscopy systems to calibrate the measured

data [28, 34]. In general, it can help extract material properties such as birefringence, diattenuation, circular dichroism, and optical activity. This formalism has even been adapted with Fourier optics to track polarization states that are sensitive to the wave vector of the light [35].

Table 3.1: List of common Jones matrices. For the linear polarizer, θ represents the angle the transmission axis makes with the x-axis. For the wave plates, θ represents the angle the fast axis makes with the x-axis. β is the difference in the phase shift between the slow and fast axis experienced by the light as it passes through the wave plate.

Optical element	**Jones matrix**
Horizontal linear polarizer	$\begin{pmatrix} 1 & 0 \\ 0 & 0 \end{pmatrix}$
Vertical linear polarizer	$\begin{pmatrix} 0 & 0 \\ 0 & 1 \end{pmatrix}$
Linear polarizer (arbitrary angle)	$\begin{pmatrix} \cos^2\theta & \sin\theta\cos\theta \\ \sin\theta\cos\theta & \sin^2\theta \end{pmatrix}$
Half wave plate	$\begin{pmatrix} \cos 2\theta & \sin 2\theta \\ \sin 2\theta & -\cos 2\theta \end{pmatrix}$
Quarter wave plate	$\begin{pmatrix} \cos^2\theta + j\sin^2\theta & (1-j)\sin\theta\cos\theta \\ (1-j)\sin\theta\cos\theta & \sin^2\theta + j\cos^2\theta \end{pmatrix}$
Wave plate (arbitrary retardation)	$\begin{pmatrix} \cos^2\theta + e^{j\Delta\beta}\sin^2\theta & (1-e^{j\Delta\beta})\sin\theta\cos\theta \\ (1-e^{j\Delta\beta})\sin\theta\cos\theta & \sin^2\theta + e^{j\Delta\beta}\cos^2\theta \end{pmatrix}$

3.1.3 Bra-ket notation

Jones calculus is also often performed using *bra-ket* notation [5]. Borrowed from quantum mechanics, this notation allows for a generalization of the Jones vector space for an arbitrary set of basis vectors. The analysis performed in this section was using a linear polarization basis, L. Another common polarization basis is circular polarizations, C, since right and

left hand circular polarizations form an orthogonal complete basis for the polarization state space. In other words, for a general polarization state $|E\rangle$, we can write

$$\langle L|E\rangle = \begin{pmatrix} E_x \\ E_y \end{pmatrix} \tag{3.18}$$

and

$$\langle C|E\rangle = \begin{pmatrix} E_+ \\ E_- \end{pmatrix} \quad . \tag{3.19}$$

The latter would be most useful for analyzing circular birefringence and circular dichroism, in which the material properties depend on the chirality of the incident light. Because linear and circular polarization states span the entire state space, we can represent a circularly polarized beam as a superposition of linearly polarized beams, and vice versa. For instance,

$$|R\rangle = \frac{1}{\sqrt{2}} \left(|H\rangle + j\,|V\rangle\right) \quad , \tag{3.20}$$

where R, H, V, represent normalized right hand circular, horizontal linear, and vertical linear polarization states respectively. Using this notation, we can conveniently write the output intensity of the optical system given by Eq 3.17 without loss of generality:

$$I_{out} = \left|\langle L|R(-\theta)|L\rangle \langle L|H|L\rangle \langle L|R(\theta)|L\rangle \langle L|S|L\rangle \langle L|H|L\rangle \langle L|E_{in}\rangle\right|^2 \quad , \tag{3.21}$$

where S represents the sample Jones matrix. This notation for Jones calculus will be used to model the experiments conducted in Chapter 4 of this work.

3.2 Stokes-Mueller formalism

3.2.1 The Stokes vector

While Jones calculus allows for convenient modeling of the polarization state of light in an optical system, it does not take into account the probabilistic nature of the polarization state over time. In other words, Jones calculus effectively tracks the polarization state of a

single photon as it propagates through various media. However, when a sample is imaged, a detector outputs a signal related to the total number of incident photons integrated over some finite integration period. Strictly speaking, a source of light is only said to be polarized if every incoming photon shares the same polarization state. On the other hand, a source of light is completely unpolarized if there is no preference for any particular polarization state over time. In the wave perspective of light, this concept can be summarized as just the degree of randomness in the phase relationship between two orthogonal components of the electromagnetic wave; in general, light will be partially polarized. First described by George Gabriel Stokes in the late 1800s, the Stokes vector captures a complete description of the polarization state of light — one that takes into account the degree of polarization. The Stokes vector is a four-dimensional vector that contain the four Stokes parameters:

$$\mathbf{S} = \begin{pmatrix} S_0 \\ S_1 \\ S_2 \\ S_3 \end{pmatrix} = \begin{pmatrix} \langle E_x^2 \rangle + \langle E_y^2 \rangle \\ \langle E_x^2 \rangle - \langle E_y^2 \rangle \\ 2 \langle E_x E_y \cos\delta \rangle \\ 2 \langle E_x E_y \sin\delta \rangle \end{pmatrix} , \tag{3.22}$$

or in terms of intensity,

$$\mathbf{S} = \begin{pmatrix} S_0 \\ S_1 \\ S_2 \\ S_3 \end{pmatrix} = \begin{pmatrix} \langle I_{0^\circ} \rangle + \langle I_{90^\circ} \rangle \\ \langle I_{0^\circ} \rangle - \langle I_{90^\circ} \rangle \\ \langle I_{45^\circ} \rangle - \langle I_{135^\circ} \rangle \\ \langle I_{LCP} \rangle - \langle I_{RCP} \rangle \end{pmatrix} . \tag{3.23}$$

The brackets here denote time averaged values and are what enable modeling of partially polarized light. For meaningful measurements, the averaging time must be much larger than the oscillation period of the electromagnetic wave. The first element, S_0, describes the total intensity. The second element, S_1, describes the tendency for the light to be linearly polarized either horizontally or vertically. The third element, S_2, similarly describes the tendency for the light to be linearly polarized in either diagonal directions (45° or 135°). Finally, the last element, S_3, describes the tendency for the light to be circularly polarized. Notice that unlike the Jones vector, the elements in the Stokes vector are all real valued, as

they all correspond to actual measured data. Another key difference is that the polarization ellipse described by the Stokes vector is not a representation of a single polarization state – but rather – is the result of a long term averaging of potentially many different polarization states over time.

Once all four Stokes parameters are known, all the quantities of interest when describing the light's polarization can be obtained. This includes the degree of polarization (DoP), orientation angle ψ, and the ellipticity angle χ. The relationship between these quantities and the Stokes parameters are given as follows:

$$\text{DoP} = \frac{\sqrt{S_1^2 + S_2^2 + S_3^2}}{S_0} \tag{3.24}$$

$$\psi = \frac{1}{2} \tan^{-1} \frac{S_2}{S_1} \tag{3.25}$$

$$\chi = \frac{1}{2} \tan^{-1} \frac{S_3}{\sqrt{S_1^2 + S_2^2}} \quad [36]. \tag{3.26}$$

For ideally polarized light, the DoP is unity, whereas completely unpolarized light would result in zero. In general,

$$0 \leq \text{DoP} \leq 1 \ . \tag{3.27}$$

It is common to also define a degree of linear polarization (DoLP) in which the circular polarization component is left out of Eq 3.24. That is,

$$\text{DoLP} = \frac{\sqrt{S_1^2 + S_2^2}}{S_0} \ . \tag{3.28}$$

3.2.2 The Poincaré sphere

The Stokes vector can also be normalized to the total intensity of the light, forming a reduced Stokes vector, $\mathbf{s}$, that contains purely polarization information:

$$\mathbf{s} = \frac{1}{S_0} \begin{pmatrix} S_1 \\ S_2 \\ S_3 \end{pmatrix} = \begin{pmatrix} s_1 \\ s_2 \\ s_3 \end{pmatrix} \ , \tag{3.29}$$

where

$$s_1^2 + s_2^2 + s_3^2 \leq 1 \quad . \tag{3.30}$$

Notice that Eq 3.30 represents a unit ball in the basis of the normalized Stokes parameters. Then, any polarization state can be visualized as a vector in three-dimensional space bounded by a unit sphere, where any point on the sphere represents completely polarized light. This geometric visualization is known as the Poincaré sphere and is shown in Fig 3.2. All points that lie along the equator of the sphere are linear polarization states, since they lack any s_3 component. The two poles represent circular polarization states with opposite handedness (north being right handed). Any point in between denotes an elliptically polarized state in which the ellipticity increases with the elevation angle, as illustrated in the figure. The azimuthal angle controls the orientation angle of the polarization, where a full revolution equates to a 180 degree rotation, which is a statement of Malus' law. Any Stokes vector that lies inside the Poincaré sphere represents partially polarized light.

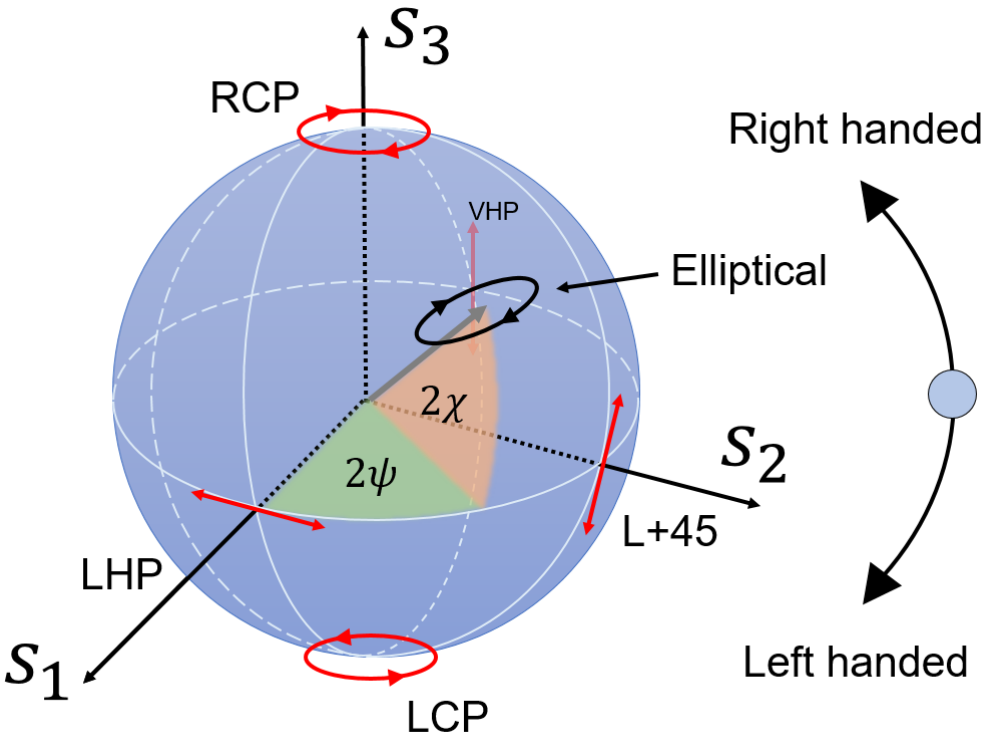

Figure 3.2: Illustration of the Poincaré sphere.

3.2.3 Mueller matrices

Through the perspective of the Poincaré sphere, it is apparent that any optical element can be interpreted as a transformation of the Stokes vector within a unit sphere. For instance, a horizontally oriented diattenuator can be thought of as a radial stretch toward the s_1 axis. A phase retarder, like a quarter waveplate, can be visualized as rotations of the sphere along a particular axis. These transformations can be written as a four-dimensional matrix operating on a Stokes vector. This is called the Mueller matrix, and it embodies all the polarization characteristics of the material including birefringence, diattenuation, dichroism, and depolarization. In general, the output Stokes vector is then

$$\mathbf{S}_{out} = \mathbf{M}_{sample}\mathbf{S}_{in} = \begin{pmatrix} m_{0,0} & m_{0,1} & m_{0,2} & m_{0,3} \\ m_{1,0} & m_{1,1} & m_{1,2} & m_{1,3} \\ m_{2,0} & m_{2,1} & m_{2,2} & m_{2,3} \\ m_{3,0} & m_{3,1} & m_{3,2} & m_{3,3} \end{pmatrix} \mathbf{S}_{in} \quad . \tag{3.31}$$

Because all Stokes vectors are real valued, each element in the Mueller matrix must also be real valued. A list of common Mueller matrices are listed in Table 3.2. Because the first row of the matrix determines the S_0 parameter of the final output Stokes vector, these elements ultimately determine the diattenuation properties of the material. If we define the diattenuation, D, as

$$D \equiv \frac{T_{max} - T_{min}}{T_{max} + T_{min}} \quad , \tag{3.32}$$

where T_{max} and T_{min} denote maximum and minimum transmittances respectively, we can write

$$D = \frac{\sqrt{m_{1,2}^2 + m_{1,3}^2 + m_{1,4}^2}}{m_{1,1}} \quad . \tag{3.33}$$

An ideal linear polarizer has a diattenuation equal to unity. The other elements in the Mueller matrix can account for any linear or circular birefringence of the material. A more detailed analysis of the elements in the Mueller matrix can be found in Ref [12]. To obtain all 16 values of the Mueller matrix in an experiment, a minimum of 16 measurements must be conducted. However, in a typical ellipsometry setup, upwards of 36 different polarization

combinations are measured to improve signal-to-noise ratios [37]. Fortunately, for many polarimetric applications, it is not necessary to measure all the elements in the sample Mueller matrix. Most polarimetric imaging is based off obtaining the four Stokes parameters of the final light output, rather than a full Mueller characterization of the interacted medium. This is the goal for the experiments demonstrated in this thesis and for many other works in polarimetric imaging [35, 11]. The four Stokes parameters can provide a means of additional contrast in an image based on the polarization, which can allow for distinctions between different objects that would otherwise be obscured in a purely intensity based image. Of course, the more information known about the illumination source and the sample material, the more the final Stokes vector can conclude about sample's Mueller matrix.

Table 3.2: List of common Mueller matrices. The parameters follow the same convention as the Jones matrices defined in Table 3.1. Reproduced from Ref [7].

Optical element	**Mueller matrix**
Horizontal linear polarizer	$\frac{1}{2}\begin{pmatrix} 1 & 1 & 0 & 0 \\ 1 & 1 & 0 & 0 \\ 0 & 0 & 0 & 0 \\ 0 & 0 & 0 & 0 \end{pmatrix}$
Vertical linear polarizer	$\frac{1}{2}\begin{pmatrix} 1 & -1 & 0 & 0 \\ -1 & 1 & 0 & 0 \\ 0 & 0 & 0 & 0 \\ 0 & 0 & 0 & 0 \end{pmatrix}$
Linear polarizer (arbitrary angle)	$\frac{1}{2}\begin{pmatrix} 1 & \cos 2\theta & \sin 2\theta & 0 \\ \cos 2\theta & \cos^2 2\theta & \sin 2\theta \cos 2\theta & 0 \\ \sin 2\theta & \sin 2\theta \cos 2\theta & \sin^2 2\theta & 0 \\ 0 & 0 & 0 & 1 \end{pmatrix}$
Half wave plate	$\begin{pmatrix} 1 & 0 & 0 & 0 \\ 0 & \cos 4\theta & \sin 4\theta & 0 \\ 0 & \sin 4\theta & -\cos 4\theta & 0 \\ 0 & 0 & 0 & -1 \end{pmatrix}$
Quarter wave plate	$\begin{pmatrix} 1 & 0 & 0 & 0 \\ 0 & \cos^2 2\theta & \cos 2\theta \sin 2\theta & -\sin 2\theta \\ 0 & \cos 2\theta \sin 2\theta & \sin^2 2\theta & \cos 2\theta \\ 0 & \sin 2\theta & -\cos 2\theta & 0 \end{pmatrix}$
Wave plate (arbitrary retardation)	$\begin{pmatrix} 1 & 0 & 0 & 0 \\ 0 & \cos^2 2\theta + \cos\Delta\beta \sin^2 2\theta & (1-\cos\Delta\beta)\cos 2\theta \sin 2\theta & -\sin\Delta\beta \sin 2\theta \\ 0 & (1-\cos\Delta\beta)\cos 2\theta \sin 2\theta & \cos\Delta\beta \cos^2 2\theta \sin^2 2\theta & \sin\Delta\beta \cos 2\theta \\ 0 & \sin\Delta\beta \sin 2\theta & -\sin\Delta\beta \cos 2\theta & \cos\Delta\beta \end{pmatrix}$

CHAPTER 4

Optical system results and characterization

In this chapter, a THz single-pixel imaging scheme is demonstrated as a testbed for polarimetric imaging. The imaging system is enabled by two main components. First is the QC-VECSEL source, which provides near-Gaussian beam shapes and high output power. Second, a motorized fast rotating linear polarizer enables extraction of Stokes parameters via lock-in detection. The first part of the chapter demonstrates the fast rotator scheme with a well known test sample. The latter portion discusses the imaging setup, its sensitivity, and imaging results. Comparisons between previous optical systems are made throughout the chapter to highlight specific achievements made in this work.

4.1 Fast rotator scheme

4.1.1 Proof of concept: waveplate measurement

The polarization sensitive detection is enabled by a fast rotator lock-in detection scheme. Fig 4.3 illustrates a simplified diagram of the optical system. The THz QC-VECSEL demonstrated in Chapter 2 is used as the illumination source. In this experiment, the laser is electrically pumped with a pulse train at a 100 kHz repetition rate (f_{fast}) and 1 μs pulse width, resulting in a 10% duty cycle. Thus, a vertically polarized terahertz beam is sent through a fast rotating linear polarizer, followed by a sample waveplate and the analyzer. The analyzer is a free-standing wire-grid polarizer (Microtech WGP G30X10-S) with its transmission axis oriented horizontally in a laboratory reference frame. The rotating polarizer is a metal wire-grid deposited on a quartz substrate mounted in a lens tube. Because

the axial ratio of the QC-VECSEL is known (see Fig 2.7), the extinction ratio (ER) of this polarizer can be well characterized using Malus' Law. The intensity measured by a pyroelectric detector as the polarizer is rotated is fitted against Eq 2.18 using least-squares under the constraints

$$\begin{aligned} \left|\frac{a_0 + a_1}{a_0 - a_1}\right| &= 100 \\ 0 \leq T_s, T_p &\leq 1 \\ T_s &> T_p \quad . \end{aligned} \tag{4.1}$$

The results are shown in Fig 4.1 with $T_s = 0.80$ and $T_p = 0.031$. The extinction ratio of this polarizer, defined as

$$ER = \frac{T_s}{T_p} \quad , \tag{4.2}$$

is calculated to be 25.8. Because this linear polarizer is used as the modulation source of the imaging system, a larger ER will produce a larger signal and a higher sensitivity to the measured polarization state. The lens tube containing the quartz mounted polarizer is fitted

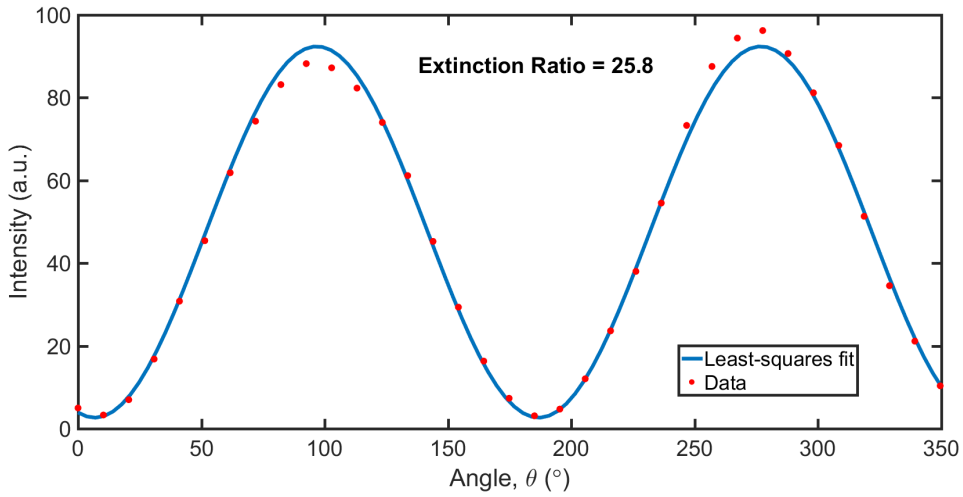

Figure 4.1: A Malus' Law measurement is performed on the quartz mounted linear polarizer used for the fast rotator. Because the axial ratio of the QC-VECSEL beam is known, the extinction ratio of the polarizer can be calculated. Based on a least-squares fit, an extinction ratio of 25.8 is obtained.

into ball bearings that rotate via a fast rotating motor (Moog Animatics SmartMotor) using

a timing belt for mechanical connection. A homemade circuit was designed to encode the rotation frequency with infrared light. The rotating linear polarizer will then act as the source of modulation for pyroelectric detection in place of electrical gating. An illustration of the modulation scheme is shown in Fig 4.2. The pulser repetition rate will continue to be labeled f_{fast}. However in the case of the rotator scheme, the encoded rotation frequency of the fast rotator will be labeled as f_{slow}. In this modulation scheme, the light intensity has a sinusoidal modulation of $2f_{\text{slow}}$ in accordance with Malus' Law.

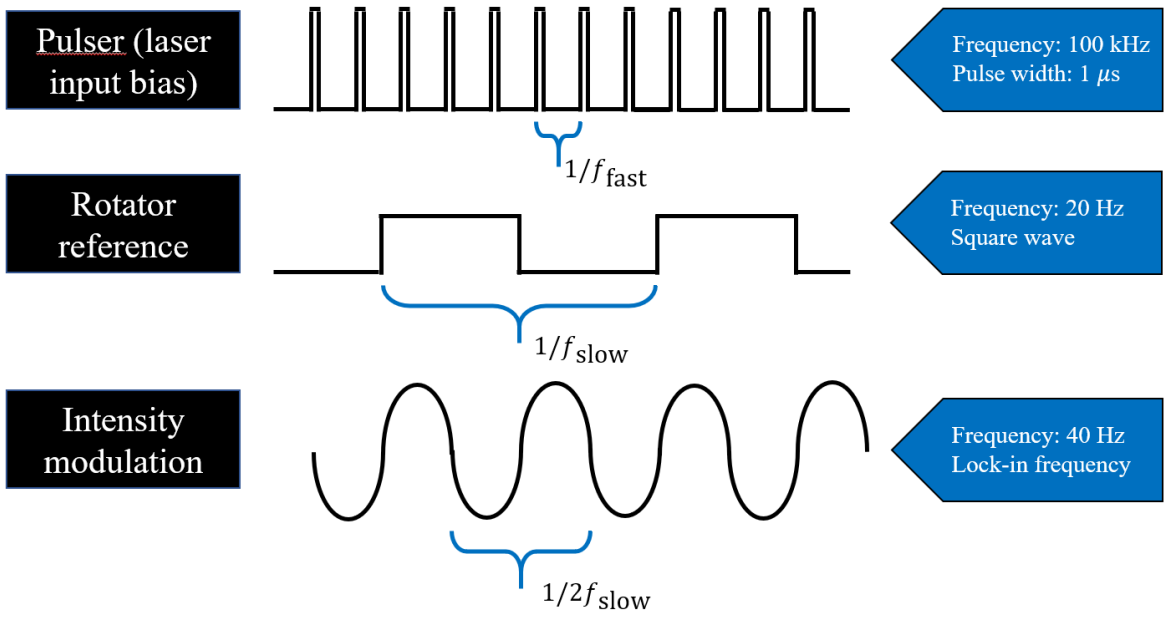

Figure 4.2: Illustration of the modulation scheme for the fast rotator imaging setup. The pulser is set at a repetition rate (f_{fast}) of 100 kHz and a pulse width of 1 μs. The rotator reference signal, produced from a homemade circuit that encodes the rotation frequency (f_{slow}), is set at 20 Hz for reasons shown later in the chapter. The intensity modulation seen by the pyroelectric detector is sinusoidal with a frequency $2f_{\text{slow}}$.

The polarization state of the output light can be modeled using Jones calculus as described in Chapter 3. The rotating scheme and the following formalism was inspired by

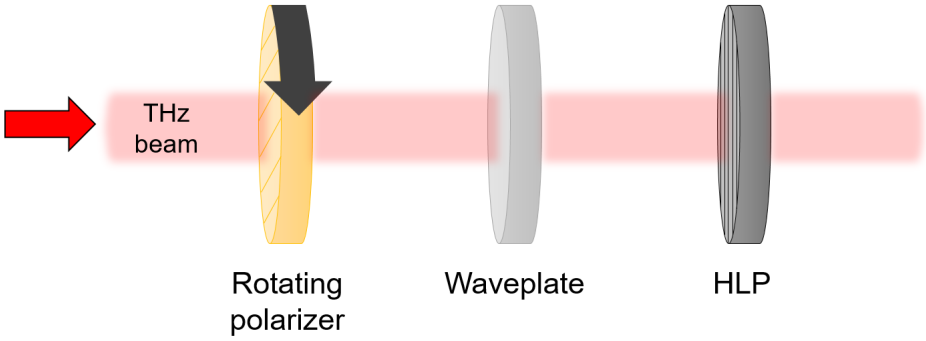

Figure 4.3: Simplified illustration of the experimental setup. The THz beam is sent through a fast rotating polarizer rotating at a frequency ω. The beam then passes through the waveplate under test followed by a linear polarizer with its transmission axis oriented horizontally.

Jenkins *et al.* in Ref [5]. Assuming a vertically polarized incident light, we have

$$\begin{aligned} \langle L|E_{out}\rangle = \langle L|R(-\omega t)|L\rangle \langle L|H|L\rangle \langle L|R(\omega t)|L\rangle \cdots \\ \langle L|R(-\theta)|L\rangle \langle L|WP|L\rangle \langle L|R(\theta)|L\rangle \langle L|V|L\rangle \langle L|E_{in}\rangle \quad , \end{aligned} \tag{4.3}$$

where ω is the angular frequency of the fast rotator, and θ is the relative angle of the waveplate. What is actually measured is the intensity, so we look at the modulus squared:

$$I_{out} = |\langle L|E_{out}\rangle|^2 \quad . \tag{4.4}$$

After some algebra, the final form of the intensity can be written as

$$I_{out} = A_{dc} + A_{2\omega,in}\cos 2\omega t + A_{2\omega,out}\sin 2\omega t + A_{4\omega,in}\cos 4\omega t + A_{4\omega,out}\sin 4\omega t \quad ., \tag{4.5}$$

where the subscripts for each coefficient represent the harmonic it is associated with. These coefficients are functions of θ and the phase retardance of the waveplate, $\Delta\beta$. By referencing frequency 2ω with a lock-in amplifier (LIA), the detected signal will only correspond to the $A_{2\omega,in}$ and $A_{2\omega,out}$ components. In particular,

$$A_{2\omega,in} = \frac{1}{2}\left[(\cos^2\theta + \cos\Delta\beta\sin^2\theta)^2 + \sin^2\Delta\beta\sin^4\theta\right] \tag{4.6}$$

and

$$A_{2\omega,out} = \frac{1}{2}\left[(\cos^2\theta + \cos\Delta\beta\sin^2\theta)(1-\cos\Delta\beta)\sin\theta\cos\theta + \sin^2\Delta\beta\sin^3\theta\cos\theta\right] \quad . \quad (4.7)$$

However, these models are only true for an ideal waveplate in which the light transmittance is unity. In general, a waveplate can have a different transmittance for its two eigen-axes. To account for this non-ideality, a term T can be introduced that represents the ratio of transmittances for its two eigen-axes. With this modification, the equations become

$$A_{2\omega,in} = \frac{1}{2}\left[(\cos^2\theta + \sqrt{T}\cos\Delta\beta\sin^2\theta)^2 + T\sin^2\Delta\beta\sin^4\theta\right] \quad (4.8)$$

and

$$A_{2\omega,out} = \frac{1}{2}\left[(\cos^2\theta + \sqrt{T}\cos\Delta\beta\sin^2\theta)(1-\sqrt{T}\cos\Delta\beta)\sin\theta\cos\theta + T\sin^2\Delta\beta\sin^3\theta\cos\theta\right] \quad . \quad (4.9)$$

A pyroelectric detector is used to detect the time-varying signal. The LIA used (SRS SR830) is a two phase detector, which means it can simultaneously detect an in-phase signal and an out-of-phase (quadrature) signal. This allows for simultaneous measurement of Eq 4.6 and Eq 4.7. The averaging time is set to 1 second, and the rotator is set to rotate (f_{slow}) at 20 Hz, with the lock-in reference frequency set to the second harmonic. A least-squares fit is performed on the total magnitude of the in-phase and quadrature component and is shown in Fig 4.4. The total phase delay of an arbitrary waveplate is

$$\phi = \frac{2\pi d}{\lambda}(n_s - n_f) \quad (4.10)$$

where n_s and n_f are the refractive indices of the fast and slow axes respectively. A fit value of $\phi = 1.94$ is obtained at $\lambda = 88\,\mu$m. The ratio of the transmittances is calculated to be about 0.67. This is in good agreement with the expected values. The waveplate was purchased from TYDEX and its parameters have already been separately tested. The waveplate is made of crystal quartz and has a measured thickness of 0.6008 mm. The indices of the fast and slow axes are given as 2.132 and 2.176 respectively, being designed for a quarter-wave plate at 115 μm. Based on the given parameters, the expected phase delay was $\phi = 1.91$

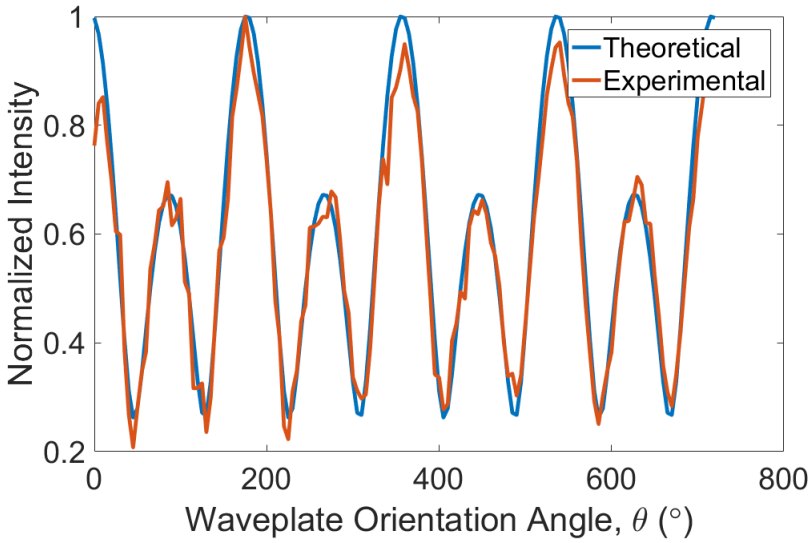

Figure 4.4: Plotted is $\sqrt{A_{2\omega,in}^2 + A_{2\omega,out}^2}$, the total magnitude of the lock-in amplifier (LIA) output. The figure shows both the obtained data and the theoretical plot for the fitted values of T and $\Delta\beta$.

with an expected transmission ratio of 0.614. Nevertheless, the signal-to-noise (SNR) ratio in this experiment was not optimized, translating to noise in the fitted values. However, as a proof of concept, a fast rotator lock-in detection scheme has been demonstrated. We can think of the fast rotator as encoding information about the material into different harmonics of the rotation frequency. These harmonics can then be individually probed with an LIA.

4.1.2 SNR dependence on chopping frequency

With a lock-in detection method, the modulation frequency of the reference signal (f_{slow}) has a significant impact on the SNR. To investigate the effects, an experiment is conducted in which the SNR of the lock-in signal is monitored over a large range of modulation frequencies. Since I wanted to study the effects of the modulation frequency on the detector alone, the modulation was achieved by electrically gating the laser bias. Indeed, the fast rotator will have its own associated noise due to vibration, mechanical jitter, and the circuit readout noise.

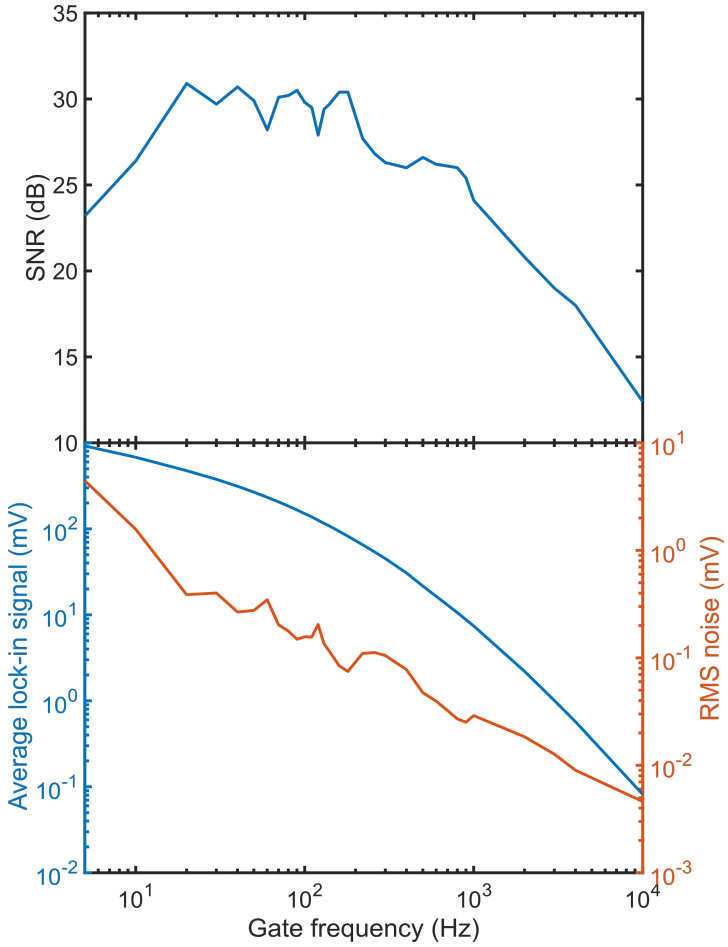

Figure 4.5: (Top) The SNR is plotted versus the gate frequency of the laser bias. Initial increase can be explained by reduction in 1/f noise. Dips in the SNR are evident at 60 Hz, 120 Hz, and 240 Hz. They are a result of the 60 Hz power line frequency. (Bottom) The average signal and the RMS noise versus the gate frequency are plotted separately. These components are used to calculate the SNR.

The SNR in decibel scale is shown in Fig 4.5 in a stacked plot showing its average signal and root-mean-square (RMS) noise constituents. We define

$$SNR = \frac{\mu_{sig}}{\sigma_{sig}} \tag{4.11}$$

where

$$\mu_{sig} = \frac{1}{N}\sum_{i=1}^{N} x_i \tag{4.12}$$

and

$$\sigma_{sig} = \sqrt{\frac{1}{N}\sum_{i=1}^{N}(x_i - \mu_{sig})^2} \tag{4.13}$$

for a sequence of N measurements given by $\{x_1, x_2, \cdots, x_N\}$. For this measurement, $N = 120$ and a sampling period of 0.5 s was used; the measurements were sampled directly from the LIA. The LIA time constant was set to 1 s for $f_{\text{slow}} \leq 10$ Hz and 300 ms for $f_{\text{slow}} > 10$ Hz. The average lock-in signal decays with the gate frequency. The pyroelectric detector can be electrically modeled as an RC circuit, where its responsivity is inversely proportional to the frequency at high frequencies. Beyond about 10^3 Hz, the signal appears to be decaying at a constant 20 dB/dec, suggesting a single-poled transfer function for the responsivity at high frequencies. This pyroelectric detector is rated to have a maximum responsivity at 5 Hz. Although not shown in this data, the detector's responsivity decays at frequencies smaller than 5 Hz, and eventually reaches zero responsivity at DC. Looking at the noise plot, there are some key features that can be highlighted. First, the noise drops quickly at low frequencies. This can mainly be attributed to decrease in the $1/f$ noise in the electronics. Second, there are local maxima located at 60 Hz, 120 Hz, and 240 Hz. These peaks are expected, as they are associated with the power line frequency (and its harmonics) in the United States. Indeed, these peaks manifest themselves as dips in the SNR. At high frequencies, the average signal decays faster than the noise, resulting in a decay in the SNR. The results suggest that the optimum modulation frequencies reside between 20 to 200 Hz, excluding frequencies near 60 and 120 Hz. While there are many other sources of noise, this experiment provides a necessary characterization of the frequency dependent noise performance of the pyroelectric detector.

4.1.3 SNR dependence on rotator frequency

In the fast rotator imaging scheme, the source of modulation is from the fast rotator, and not an electrical gate. The instability of the rotator gets worse with increasing frequency. A similar measurement of the SNR was performed with this modulation scheme and is shown

in Fig 4.6. For this measurement, an LIA time constant of 1 s was used with a sample periodicity of 2 s for $N = 60$ samples. The results show that unlike the case of electrical modulation, the noise increases with the modulation frequency. As a result, the SNR almost monotonically decreases. While the data suggests an optimum rotation frequency (f_{slow}) of 5 Hz, there is a tradeoff between the modulation frequency and the data acquisition rate. The integration time must be many times greater than the periodicity of the modulation; a 5 Hz modulation would require averaging times on the order of seconds. Based on the data, a rotation frequency of 20 Hz is used for imaging allowing for an LIA integration time constant of 300 ms. Note that this data was collected before additional improvements were made to the SNR — as will be described in the later sections.

4.2 Single pixel imaging system

4.2.1 Experimental setup

An optical system that employs the fast rotator lock-in scheme is constructed. A schematic of the setup is shown in Fig 4.7. The goal is to accurately measure the polarization state of the light transmitted through an arbitrary sample and form an image based on this information. As before, the VECSEL is pumped with a pulse train set at a 100 kHz repetition rate (f_{fast}) and 1 μs (10% duty cycle). A high-resisivity (HR) silicon lens is used due to its high transmittance at this frequency. The lens, with a focal length of 1 in, focuses down the beam onto the sample. The sample is mounted on a XY translational stage for raster scanning. The beam then goes through the fast rotator rotating at an angular frequency ω. Off-axis parabolic mirrors (OAPs) are used to collimate the beam and refocus it onto the pyroelectric detector. The OAPs are used to avoid using additional lenses that will introduce more loss in the system. While OAPs have been shown to distort the polarization of THz beams, any polarization distortions that occur after the fast rotator is not as important as the polarization information that gets stored into the beam's intensity [38]. Finally, the detector signal is read out by the LIA's in-phase and quadrature components. Previous setups

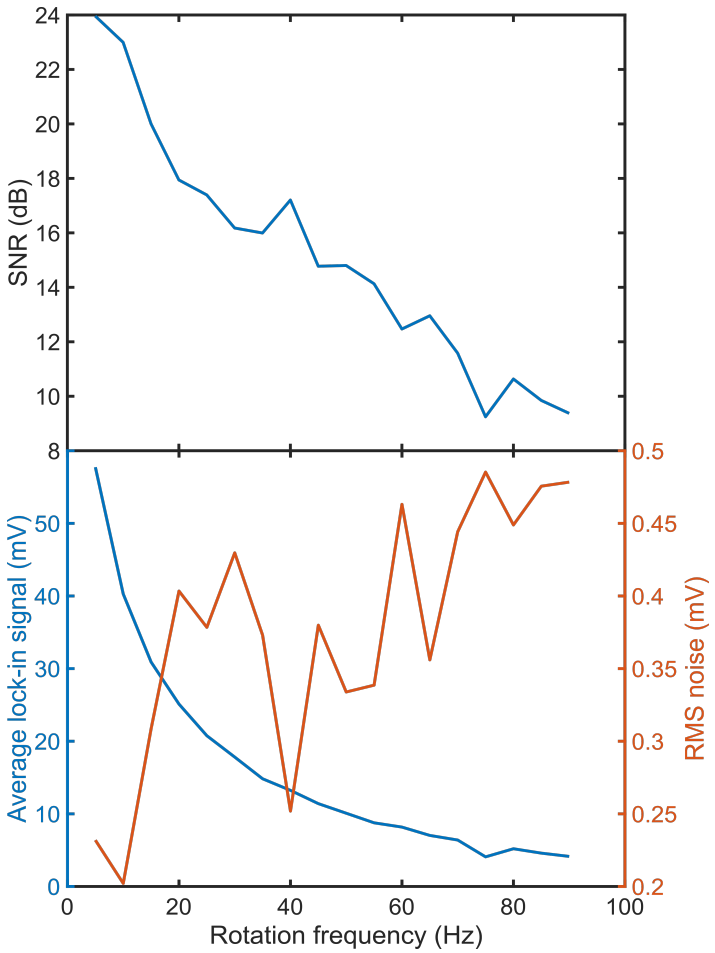

Figure 4.6: (Top) The SNR is plotted versus the rotation frequency of the fast rotator. The SNR is almost monotonically decreasing throughout the entire frequency sweep. (Bot) The average signal and noise components of the SNR are plotted separately. Contrary to the results from the electrical modulation test, the noise increases with the rotation frequency here. This is because the noise from the instability of the mechanical rotator dominates other sources of noise.

employed two TPX lenses for both focusing and detection without any OAP mirrors. These systems showed considerably worse SNR due to substantial losses from the TPX material. An optical system involving only OAPs were also tested. While the signal strength improved, the beam focused by an OAP mirror showed considerable distortion and larger spot size.

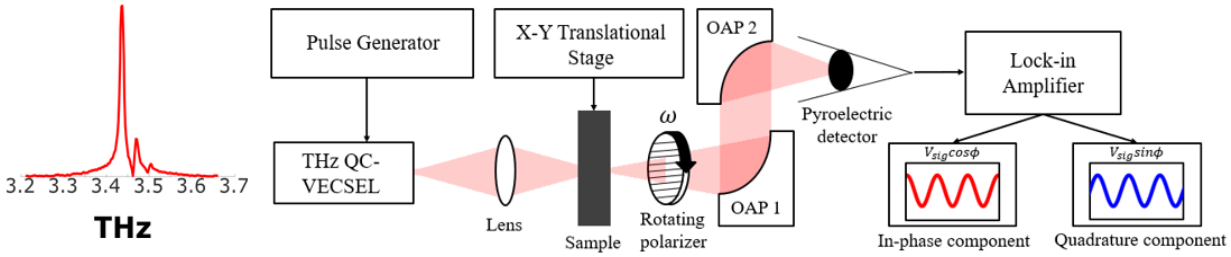

Figure 4.7: Schematic of single-pixel imaging setup.

4.2.2 SNR and sensitivity

To improve the SNR of the imaging system, we must increase the average signal and reduce the noise. To increase the average power detected, the laser is biased near the maximum current density. It is also desired to push the duty cycle as far as possible, but it was demonstrated in Chapter 2 that increasing the duty cycle introduces heating effects that will eventually decrease the power output. Based on this information, a 10% duty cycle was chosen. Maximizing power detected also means to minimize loss in the optical system. Gold coated OAPs are used to collect the beam after the fast rotator for their near unity reflectivites in the terahertz [39]. To minimize loss in the HR silicon lens, the lens was Paralyne coated on both sides for anti-reflection (AR) coating. For an ideal anti-reflective coating, the following conditions must be met:

$$n_c = \sqrt{n_{sub}} \quad . \tag{4.14}$$

and

$$t_c = \frac{(2m+1)\lambda_0}{4n_c} \quad \text{for} \quad m = 0,\ 1,\ 2,\ \cdots \quad . \tag{4.15}$$

where n_c and t_c represent the index of refraction and thickness of the coating respectively. n_{sub} is the index of the substrate which in this case is high-resistivity silicon. Based on Eq 4.14, the ideal index for the AR coating is about 1.85 for this substrate which has an index of 3.4175 at the desired 3.44 THz target frequency [6]. Paralyne C comes close with an index of about 1.62 [40]. However, the deposition rate is less controlled, making it difficult

to achieve a target thickness. The coating was performed in the UCLA Nanoelectronics Research Facility cleanroom with a vacuum deposition process. The target thickness for the desired frequency, 3.44 THz, is about 13.43 μm. A 280 μm thick HR silicon wafer was coated during the same deposition run as a means to measure the thickness of the coating via Fourier transform infrared (FTIR) spectroscopy. A transmission spectrum of the HR silicon wafer before the coating is shown in Fig 4.8(a). The measurement was performed using a liquid Helium cooled Ge:Ga photodetector and with a spectral resolution of 0.25 cm^{-1}. The occasional spikes in the measurements are caused by atmospheric absorption lines that can get substantial in this frequency range – especially due to water absorption.

To simulate the transmission spectra of the AR coated silicon, we must also consider the absorption coefficients of the coating and the substrate. These parameters have already been well characterized by previous studies [6, 40, 41]. The absorption coefficient for Paralyne C can be modeled by

$$\alpha_c = 0.006\nu - 0.7 \ . \tag{4.16}$$

where ν is the frequency in GHz. At 3.44 THz, this absorption coefficient becomes 20 cm^{-1}. The absorption coefficient for silicon is shown in the inset of Fig 4.8(b) and was reproduced from the measurements conducted in Ref [6]. For silicon, the absorption coefficient is about 0.13 cm^{-1} at the target frequency. Because the silicon substrate used is relatively thin, the absorption from Paralyne will dominate that from silicon. After the deposition, the coating thickness was measured to be about 11.8 μm, which hits a frequency of 3.92 THz. Plotted in Fig 4.8(b) is the calculated transmission spectra for the measured thickness, the measured transmission spectra, and the calculated transmission spectra for the target frequency. While the target was not exactly met, we see that the transmission still drastically improved compared to the case without AR coating. The laser frequency is shown in the figure marked with the dashed vertical line at 3.44 THz. Additionally, parts of the measured spectrum seem to go above 100% transmission, suggesting there may have been some alignment issues in the FTIR when the sample was inserted. The actual transmission values should be lower and closer to that of the simulated data to reflect the loss; still, it can be seen that the Par-

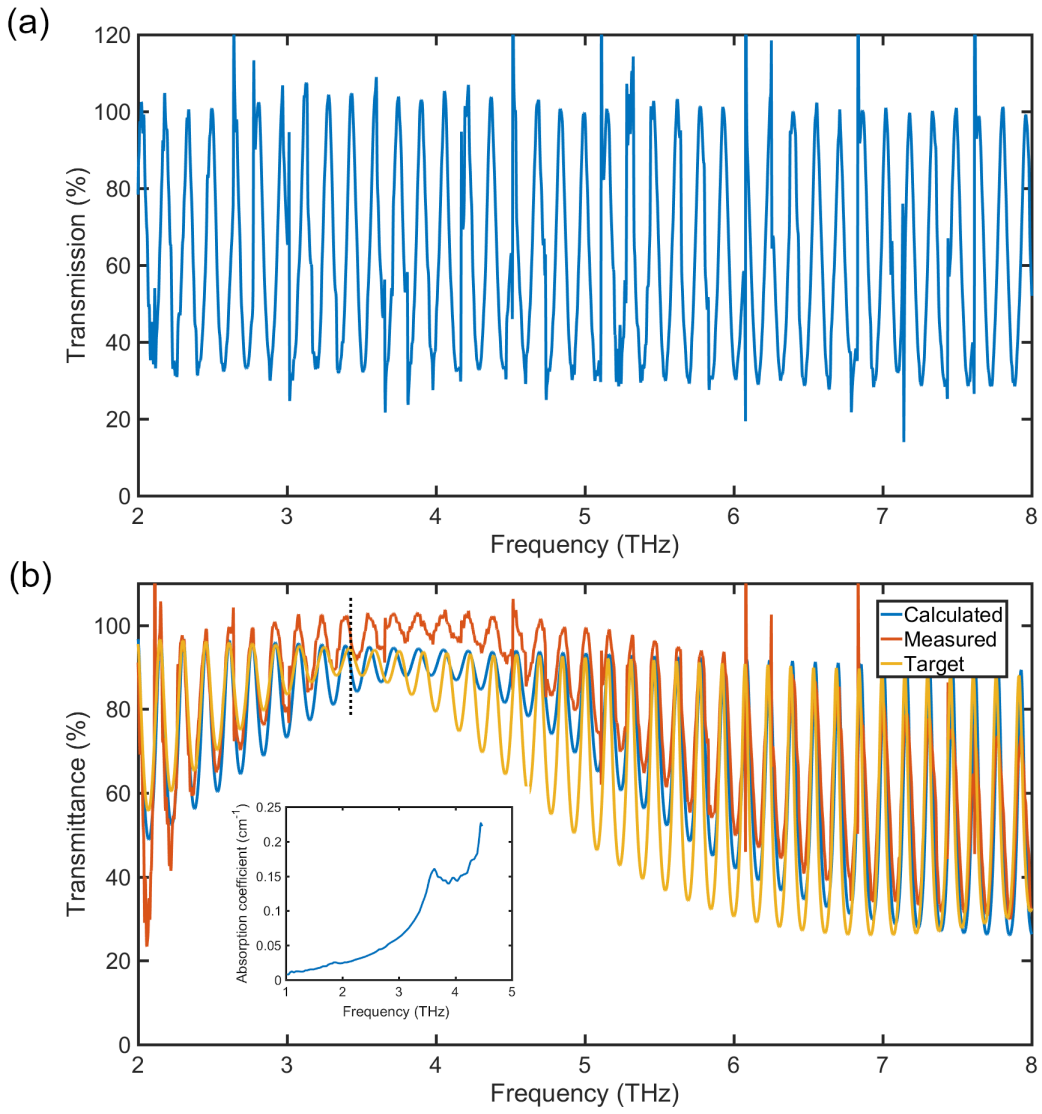

Figure 4.8: (a) Transmission spectrum of the 280 μm thick HR silicon substrate before the AR coating. The measurement was performed with an FTIR spectrometer using a liquid Helium cooled Ge:Ga photodetector and a spectral resolution of 0.25 cm^{-1}. (b) The orange curve shows the transmission spectrum of the AR coated silicon sample. The blue curve is a simulated spectrum for the measured thickness of 11.8 μm. The yellow curve is the simulated spectrum for the target thickness of 13.43 μm shown by the dashed vertical line. The inset shows the absorption coefficient for HR silicon from 1-4.5 THz reproduced from Ref [6].

alyne AR coating helps substantially improve the transmission through HR silicon despite the imperfectly matched index of refraction. The coating boosted the average signal level of our imaging system by about 50%, agreeing with the results from Fig 4.8.

Methods to reduce noise are also employed. A high-density polyethylene filter for the pyroelectric detector can help reduce the black-body radiation noise and stray light from the background. While the dependence on the modulation frequency was characterized in the previous sections, the mechanical noise produced by the rotator must also be considered here. Rotation frequencies (f_{slow}) beyond 50 Hz would increase the instability of the rotator. With these considerations, a rotation frequency of 20 Hz was chosen, resulting in a lock-in frequency of 40 Hz. While there are other noise sources such as the noise in the laser bias and the relative intensity noise, the noise from the fast rotator appears to be the dominant factor. With the rotator setup and an averaging time of 300 ms, an SNR of 31.5 dB was achieved.

A before and after comparison of the SNR is shown in Fig 4.9. Fig 4.9(a) shows a measured SNR taken much earlier in the development. Instead of an AR coated HR silicon lens with OAP mirrors, two TPX lenses were used for both focusing and detection. Fig 4.9(b) shows the SNR obtained for the current imaging setup including the additions detailed in this section. Both measurements were obtained at a 20 Hz rotation frequency with an LIA time constant of 300 ms. All measurements were performed with the QC-VECSEL biased near the maximum current density (660 A/cm^2) at a 10% duty cycle (100 kHz repetition rate, 1 μs pulse width). The SNR was improved by about 9 dB. As will be shown later in this chapter, this resulted in an order of magnitude increase in the polarization sensitivity of the imaging system.

4.2.3 Spatial resolution

The spatial resolution of this imaging system is determined by the spot size achieved at the sample. To model the minimum spot size of the beam after the lens, we can employ Gaussian

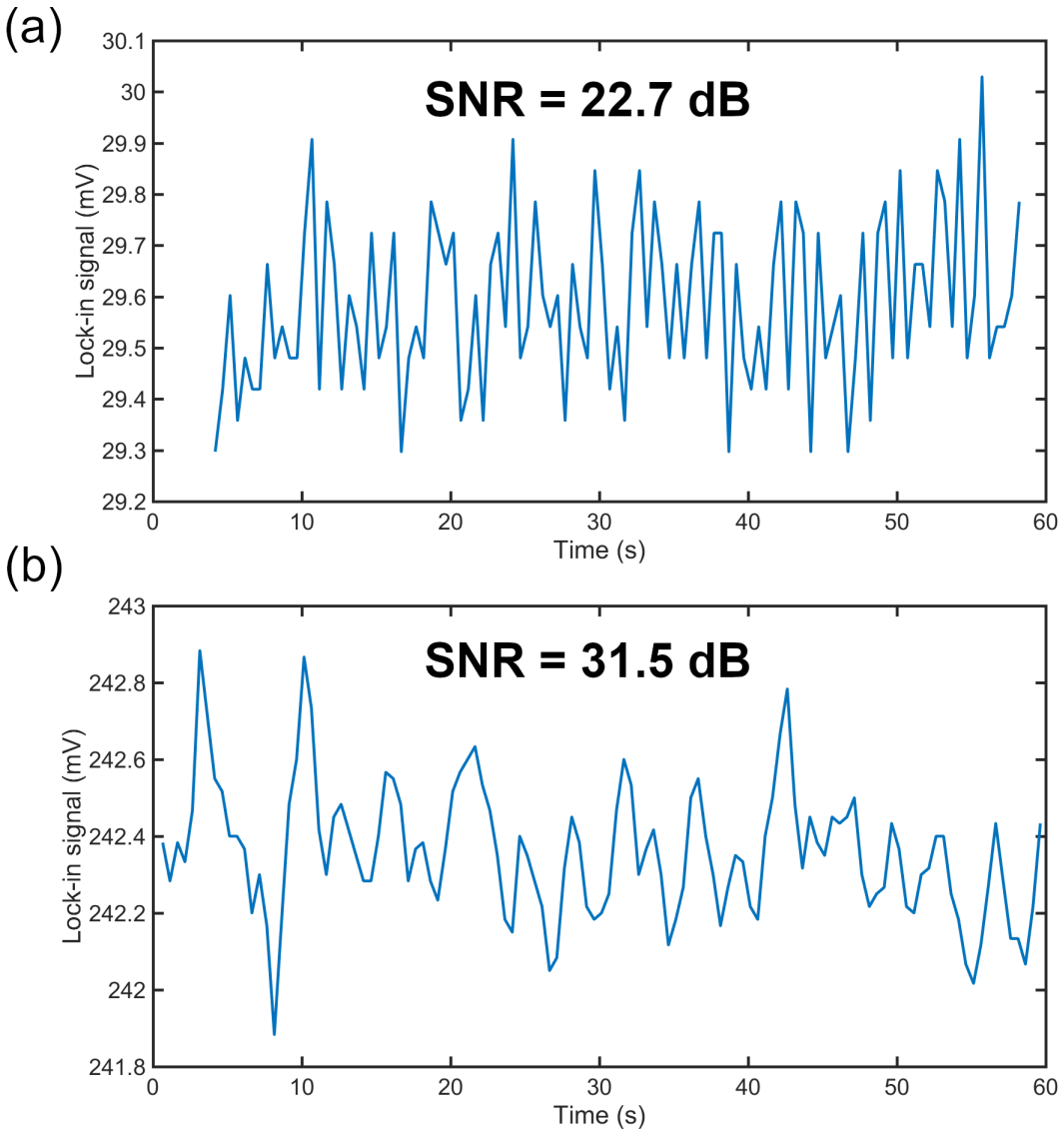

Figure 4.9: (a) Old setup involving two TPX lenses without the use of OAP mirrors. The SNR was calculated over a 60 second time interval with an LIA integration time constant of 300 ms. (b) The same measurement performed for the current setup using an AR coated HR-Si lens to focus the beam and OAP mirrors to collect the beam.

ray tracing as described in Ref [42]. For a Gaussian beam, we can define

$$\frac{1}{q(z)} = \frac{1}{R(z)} - j\frac{\lambda}{\pi w^2(z)} \tag{4.17}$$

where $R(z)$ is the radius of curvature and $w(z)$ is the beam radius. With this complex beam parameter $q(z)$ defined, it can be used with traditional ABCD matrix calculations in ray

tracing. The ABCD matrix for a given optical element acts as a transformation to the initial complex beam parameter $q_1(z)$. That is,

$$\frac{1}{q_2(z)} = \frac{C + D(1/q_1)}{A + B(1/q_1)} \quad . \tag{4.18}$$

From traditional optics, we know that the ABCD transmission matrix for a lens plus a propagation distance z is given by

$$\mathbf{T} = \begin{pmatrix} 1 - \frac{z}{f} & z \\ -\frac{1}{f} & 1 \end{pmatrix} \tag{4.19}$$

where f is the focal length of the lens. Based on this, we can calculate the beam radius at any point after the lens:

$$w^2(z) = \frac{\lambda z_1}{\pi} \left[\left(1 - \frac{z}{f}\right)^2 + \left(\frac{z}{z_1}\right)^2 \right] \tag{4.20}$$

where

$$z_1 = \frac{\pi w_1^2}{\lambda} \tag{4.21}$$

and w_1 is the radius of the beam incident on the lens. With this, we can finally calculate the minimum spot size achievable after focusing:

$$w_{min} = \frac{4}{3} \left(\frac{\lambda f}{\pi w_1} \right) \quad . \tag{4.22}$$

Notice that the larger the beam is when incident on the lens, the smaller the spot size can be. The lens is placed 5 inches from the output coupler of the QC-VECSEL. Using Eq 4.22, the minimum beam radius is calculated to be $w_{min} \approx 0.2$ mm, or a 0.4 mm beam diameter. These values are obtained for an ideal Gaussian beam. The M^2 performed in Chapter 2 allows for calculation of a more realistic beam diameter of about 0.75 mm.

However, spatial resolution in imaging is not generally defined by the beam spot size. Instead, the spatial resolution is often quantified with how well the imaging system can distinguish between two adjacent objects. In other words, as long as there exists sufficient contrast, then the image system is said to be able to resolve the features. A test was conducted in a separate measurement without the fast rotator and a polymethylpentene

(TPX) lens instead of a HR silicon lens. A convenient way to characterize the spatial resolution is by imaging a 1951 USAF resolution test chart, as shown in Fig 4.10(a). The test chart has an array of line pairs with varying dimensions that are standardized. By imaging these line pairs, the test chart effectively characterizes the spatial frequency response of an imaging system. As the line pairs become smaller, so does the contrast. If we define the contrast as

$$\text{Contrast}(\%) = \frac{I_{max} - I_{min}}{I_{max} + I_{min}} \times 100\% \ . \tag{4.23}$$

where the maximum and minimum intensity values are taken from the bright and dark spots of each line pair, the spatial resolution of an imaging system can be characterized by the largest number of line pairs that can be resolved per unit length before reaching zero contrast. A cross-section intensity profile indicated by the black line in the USAF image is show in Fig 4.10(b).

By calculating the contrast for the different size line pairs, the modulation transfer function for the imaging system is plotted (Fig 4.10(c)). The blue curve corresponds to the measurements of the horizontal line pairs, which give vertical spatial frequencies. Likewise, the red curve corresponds to measurements of horizontal spatial frequencies. The results show that there is lack of transverse symmetry in the spatial resolution between the orthogonal horizontal and vertical components. This is possible if the beam shape is not radially symmetric (circular), however the beam shape is well known from previous measurements shown in Chapter 2. The more likely explanation is because the laser beam is nearly linearly polarized. The USAF target used was metal to allow for transmission mode testing, which would cause a polarization dependent response at small length scales; the line pairs essentially act as local wire-grid polarizers. The beam is vertically polarized in the laboratory reference frame, so the vertical line pairs would would have a smaller overall transmission. Another factor could be owed to spherical abberations of the focusing lens. Nevertheless, the modulation transfer function has a cut-off frequency of about 3.5 lp/mm for both directions. The line pairs that correspond to this dimension are shown in Fig 4.10(a) with a white dashed oval. Indeed, the lines cannot be distinguished at this scale.

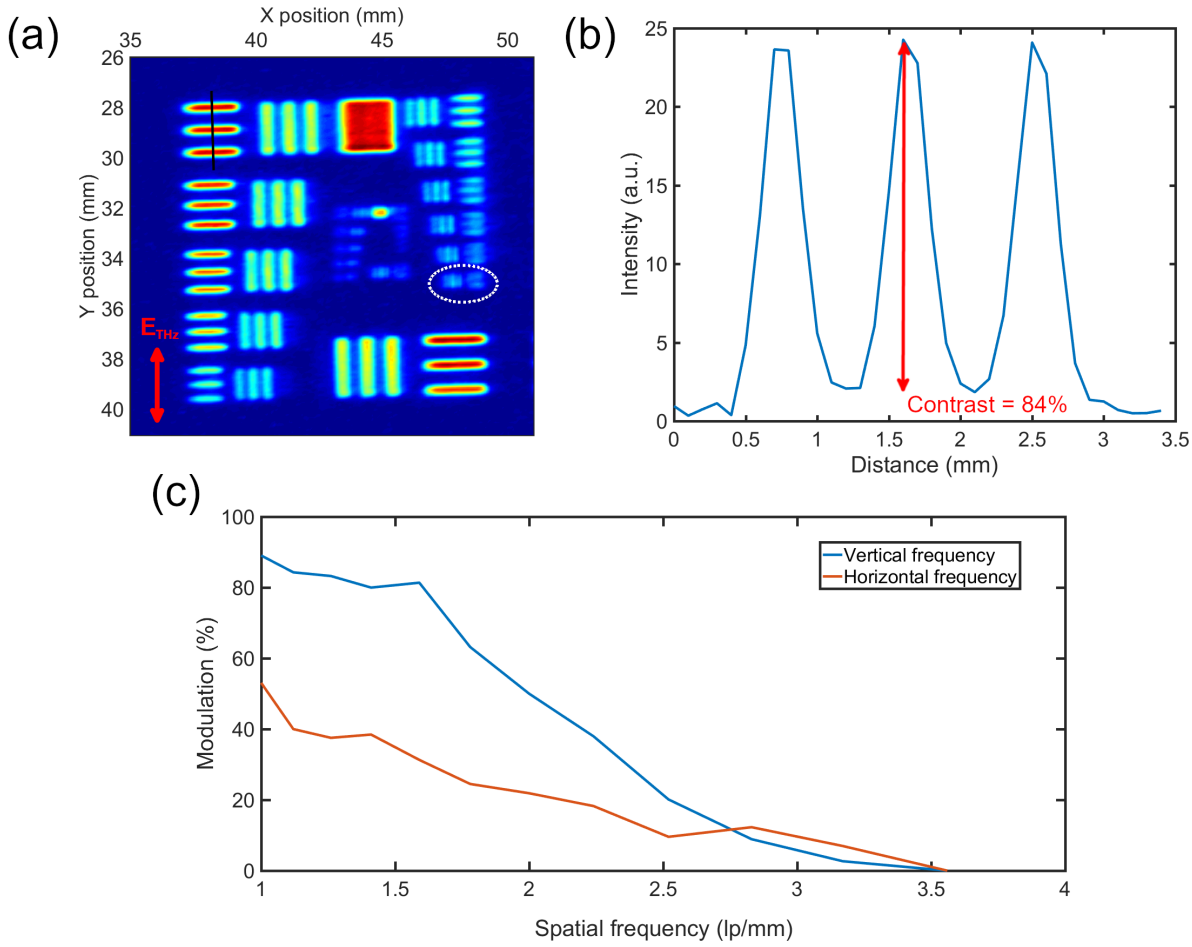

Figure 4.10: (a) Transmission mode image of 1951 USAF resolution test chart. The targets begin from group 0 and end with group 3. The image was raster scanned with a 0.1 mm step size and 300 ms averaging time. The double-headed arrow indicates the polarization state of the incident beam. (b) A sample cross-sectional intensity profile of the line pairs indicated by the black line in the target image. A contrast of 84% is measured. (c) Modulation transfer function obtained from (a). The blue curve corresponds to the horizontal line pairs whereas the red curve corresponds to the vertical ones. Both have a cutoff frequency of about 3.5 lp/mm.

The modulation transfer function characterizes the spatial resolution with a little more meaning than the beam spot size alone. This is because the size of the beam can be larger than the features of an object, but still be able to resolve them. We can think of the

line targets as a way of extracting the line-spread function of the system, which is a linear integration of the point-spread function. It is only when the point-spread functions overlap to the point in which their peaks cannot be differentiated that defines resolution limit. This is analagous to Abbe's description of diffraction limited spatial resolution.

A comparison of the USAF target images between previous imaging setups and the more current setup is shown in Fig 4.11. Fig 4.11(a) is taken with an OAP mirror as the focusing element. While removing the lenses increases the total signal strength, the spatial resolution becomes considerably worse when using OAPs. The spot size at the focal point is larger and also leads to asymmetric beam profiles. A dramatic improvement can be seen in Fig 4.11(b) where the only change was using only TPX lenses (one to focus and one to collect) instead of OAP mirrors. The step size for both these measurements were 0.2 mm and an LIA integration time constant of 1 s. However, using two TPX lenses introduces a lot of loss. According to Ref [43], the absorption coefficient of TPX at 3.4 THz is 1.1 cm^{-1}. The TPX lenses are 10 mm thick at the center. This results in a transmittance of about 77% through each lens. The low SNR obtained from using two TPX lenses becomes more evident in Fig 4.11(c), where a smaller integration time of 300 ms is used. By using a TPX lens to focus the beam, but OAP mirrors to collect the power for detection, we are able to achieve high spatial resolution while maintaining good SNR (as shown in Fig 4.11(d)). Further improvement is visible when using the AR coated HR silicon lens.

4.2.4 Stokes-Mueller modeling

The optical system as shown in Fig 4.7 can be modeled with Stokes-Mueller formalism. The formalism has been described in Chapter 3 as a way of conveniently tracking the full polarization description of light. The Stokes vector output of the single-pixel imaging setup shown in Fig 4.7 is given by

$$\mathbf{S}_{out} = \mathbf{M}_{rotator}\mathbf{M}_{sample}\mathbf{S}_{in} \quad , \tag{4.24}$$

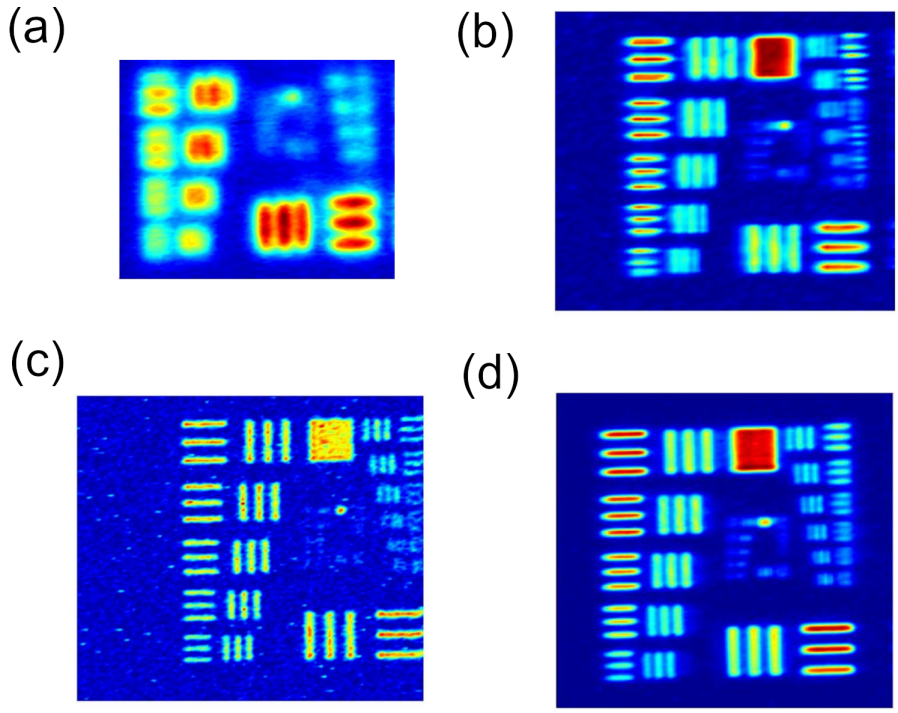

Figure 4.11: (a) Focused and collected by OAP mirrors without the use of any lenses. A 0.2 mm step size is used with a 1 second integration time. (b) Focused and collected by TPX lenses without the use of any OAP mirrors. A 0.2 mm step size is used with a 1 second integration time. (c) Same setup as that in (b) except a 0.1 mm step size is used with a 300 ms integration time. (d) A single TPX lens to focus followed by OAPs for collection. A 0.11 mm step size is used with a 300 ms integration time.

where $\mathbf{M}_{rotator}$ is the Mueller matrix of the fast rotator and $\mathbf{M}_{sample}$ is that for an arbitrary sample. From Table. 3.2, we know that

$$\mathbf{M}_{rotator} = \frac{1}{2}\begin{pmatrix} 1 & \cos 2\omega t & \sin 2\omega t & 0 \\ \cos 2\omega t & \cos^2 2\omega t & \sin 2\omega t \cos 2\omega t & 0 \\ \sin 2\omega t & \sin 2\omega t \cos 2\omega t & \sin^2 2\omega t & 0 \\ 0 & 0 & 0 & 1 \end{pmatrix} . \tag{4.25}$$

Since the main goal is to determine the polarization state of the light after propagation through the sample, we will define

$$\mathbf{S}_{sample} = \mathbf{M}_{sample}\mathbf{S}_{in} = \begin{pmatrix} S'_0 \\ S'_1 \\ S'_2 \\ S'_3 \end{pmatrix} \quad . \tag{4.26}$$

Then, the output Stokes vector is given by

$$\mathbf{S}_{out} = \mathbf{M}_{rotator}\mathbf{S}_{sample} = \frac{1}{2}\begin{pmatrix} S'_0 + S'_1\cos 2\omega t + S'_2 \sin 2\omega t \\ S'_0\cos 2\omega t + S'_1\cos^2 2\omega t + S'_2 \sin 2\omega t \cos 2\omega t \\ S'_0\sin 2\omega t + S'_1\sin 2\omega t \cos 2\omega t + S'_2 \sin^2 2\omega t \\ S'_3 \end{pmatrix} \quad . \tag{4.27}$$

Since the first element describes the total intensity, the final light intensity that arrives at the pyroelectric detector is

$$I_{out} = \frac{1}{2}\left(S'_0 + S'_1\cos 2\omega t + S'_2 \sin 2\omega t\right) \quad . \tag{4.28}$$

Based on this equation, we can readily see what can and cannot be measured from the imaging setup. The S'_1 and S'_2 components are simultaneously obtained by locking into the 2ω reference frequency; the LIA actually outputs RMS values, but this distinction is unimportant in this experiment. Thus, Eq 3.25 provides the relative angle of polarization at every point. Secondly, Eq 4.28 demonstrates that any circular polarization components of the light does not show up in the intensity. However, because the incident beam is near linearly polarized, the S'_3 component will be negligible for most samples. Additionally, the S'_0 term is a DC signal and cannot be detected, since the pyroelectric detector only responds to AC inputs. As a result, this scheme does not allow for measuring the degree of polarization. While this is achievable with modifications to the imaging setup, more optical elements will need to be added, bringing in more insertion loss. For the purposes of this experiment, we focus on images based on the angle of polarization and discuss if there exists any additional information that an intensity based image alone does not provide.

4.2.5 Imaging results and discussion

An image of a plastic cap from a small wafer container is produced from the single-pixel imaging system and is shown in Fig 4.12. To speed up acquisition, a slightly larger step size of 0.2 mm was used. The spot size at the focal point was measured to be 0.45 mm. The overall image dimension is about 20 × 25 mm. Fig 4.12(a) shows a photo of the imaged sample. The red circle indicates the region in which the sample was scanned. Fig 4.12(c) is an image in which the pixel values represent a relative rotation angle of the linear polarization state given by Eq 3.25. Thus, the image shows

$$\psi_{rot} = \frac{1}{2}\tan^{-1} S_2'/S_1' \quad . \tag{4.29}$$

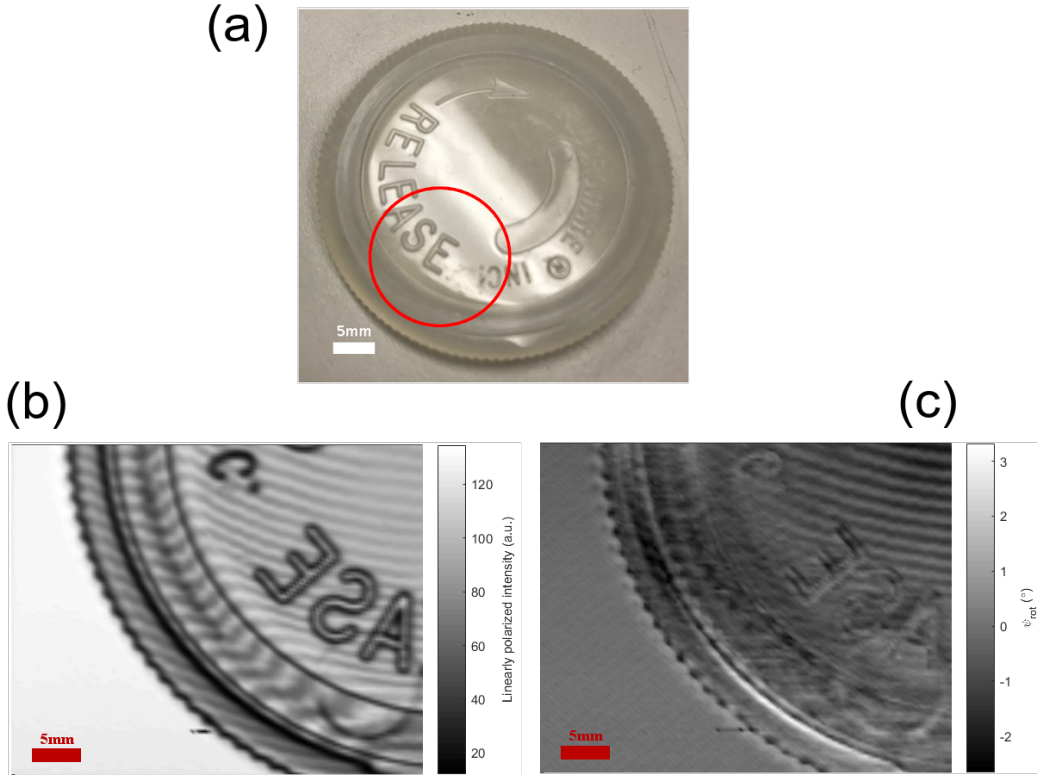

Figure 4.12: (a) Photo of sample image. The red circle indicates the region in which the image is scanned. (b) Image based on the linearly polarized intensity, I_{LP}, obtained from Eq 4.30. Interference fringes are clearly visible throughout the sample. (c) Image produced from the relative angle of polarization, ψ_{rot}, obtained from Eq 4.29.

To compare this image with an intensity-based one, an image of the total linearly polarized intensity is shown in Fig 4.12(b). The total linearly polarized intensity is given by

$$I_{LP} = \sqrt{(S_1')^2 + (S_2')^2} \ . \tag{4.30}$$

For light that is linearly polarized, this would be equal to the total intensity. To characterize the sensitivity of this imaging system to polarization angles, a separate measurement was performed in the absence of a sample. By applying Eq 4.29 to a continuous measurement without a sample, we can quantify how the noise of the system propagates into noise in the measured rotation angle. This noise equivalent rotation angle (NERA) is measured over a 60 second time interval with an LIA time constant of 300 ms. Fig 4.13 shows a comparison once again of the NERA obtained between a previous setup and the current setup as was done in Fig 4.9. An NERA of 0.30 mrad/$\sqrt{\text{Hz}}$ is measured for the current setup, which is almost an order of magnitude increase in the polarization sensitivity compared to the older setup.

By setting the relative phase of the lock-in reference signal such that $S_2' = 0$, the reference (background) polarization angle can be set to 0°. A few observations can be made comparing the two images:

1. The ψ_{rot} image washed out most of the interference fringes present in the I_{LP} image. This is because they are intensity based phenomena during transmission mode measurements. This is especially apparent throughout the raised inner ring where almost all the fringes are gone.

2. With the interference fringes washed out, the ψ_{rot} image more clearly highlights the geometrical features of the sample without obscuring artifacts.

3. The dark ring near the outer circumference in the I_{LP} where light got significantly attenuated does not say much about what caused that attenuation. However the corresponding regions in the polarization image indicate strong polarization rotation up to 3°. This suggests there is strong scattering in this region, indicating sharp edge features.

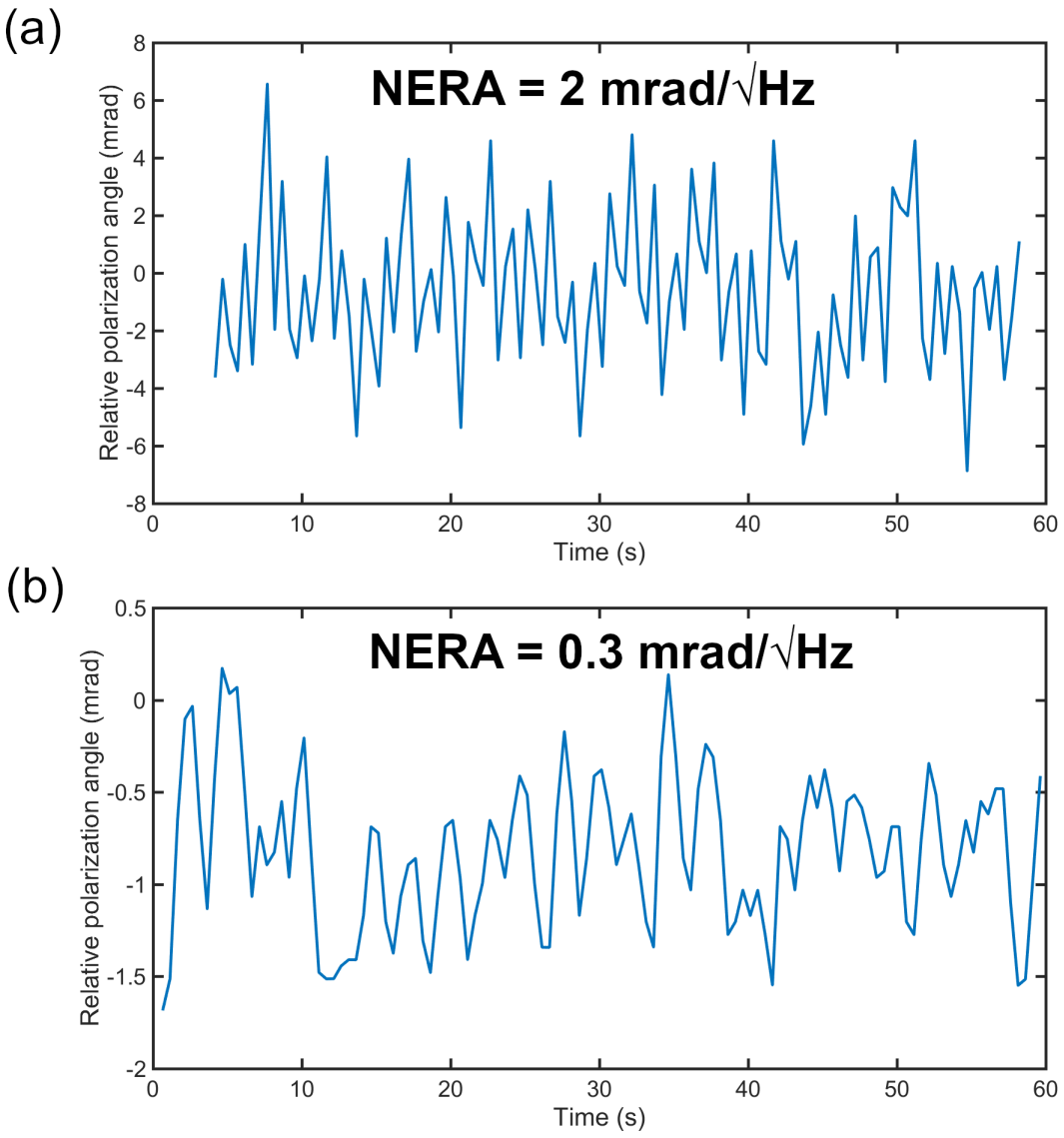

Figure 4.13: (a) Old setup involving two TPX lenses without the use of OAP mirrors. The NERA was calculated over a 60 second time interval with an LIA integration time constant of 300 ms. (b) The same measurement performed for the current setup. An order of magnitude improvement in the polarization sensitivity is observed.

4. The ψ_{rot} image has a slight periodic oscillation along a diagonal direction. This is an artifact produced by the fast rotator readout circuit that has since been fixed.

To explore further the observations made here, another set of images was taken on different plastic cap in which an area was roughened with 80 grit sandpaper. If the surface roughness

is characterized by a random distribution on the scale of the spot size, the sample will be depolarizing [44]. It follows that any non-random contribution from surface roughness, such as that from macroscopic scratches, have localized Fresnel coefficients based on their geometry that can result in a net rotation in the polarization angle. Fig 4.14 once again shows both the intensity based image and the polarization orientation image. Similar observations can be made here. However, the roughened features are more distinctly highlighted in Fig 4.14(b) in which a polarization rotation up to 7° is observed. Looking under a microscope, the lines that show sharp contrast in this image corresponded to particularly deep scratches in the plastic. Additionally, the interference fringes are completely washed out in this case as expected.

These results are not too surprising, since it is well known that light scattered from various geometries can have strong signatures in their polarization state. However performing the imaging in terahertz can take advantage of the frequency's high transmission to common plastics and its smaller wavelength compared to microwaves. In fact, there has been extensive research in imaging plastics and polymers due to these advantages [45]. Indeed, the results shown here can be extended to reflection mode imaging for applications such as non-destructive evaluations of paintings and coatings. Polarimetric information in such scenarios could provide important information about the surface such as corrosion in metals.

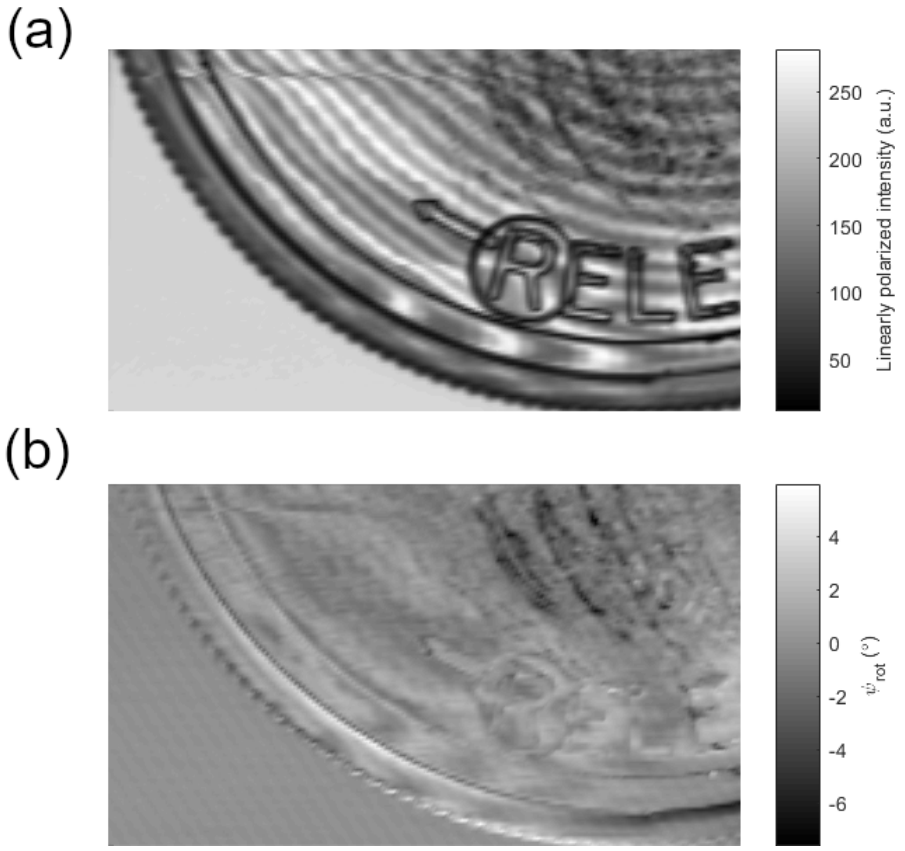

Figure 4.14: A plastic cap was roughened with 80 grit sandpaper on the upper right region of each image. (a) Image based on linearly polarized intensity, I_{LP}. (b) Image based on the relative angle of polarization, ψ_{rot}. The roughened feature has much higher contrast and is highlighted in this image. A rotation up to -7° is observed. Additionally, the interference fringes from (a) are no longer visible.

CHAPTER 5

Conclusion

In this thesis work, I have demonstrated a prototype THz imaging setup is demonstrated as a testbed for polarization sensitive imaging. It has also been shown that the QC-VECSEL architecture has several advantages for a single-pixel imaging setup such as near-Gaussian beam pattern and high output power. The mathematical formalism in describing the polarization state of light was demonstrated in detail. This formalism was used to help obtain the final Stokes vector measured by the optical system. The presented imaging system achieved a noise equivalent polarization rotation angle of 0.30 mrad/$\sqrt{\text{Hz}}$ with an SNR of 31.5 dB. A spatial resolution with a cutoff frequency at 3.5 lp/mm was observed, enabled by the shorter wavelength compared to the microwave and the high quality beam pattern produced by the QC-VECSEL. This project was inherited from a previous graduate researcher, and particular improvements were made to the optical system including:

1. A characterization of the noise dependency on the modulation frequency of the rotator. It was observed that the rotator was the dominant source of noise and thus changes were made to the mechanical design and circuit to improve overall stability. The stability has since been further improved by replacing the homemade encoder circuit with a clock signal produced from the SmartMotor (Moog Animatics).

2. Elimination of the lossy TPX lenses and instead using an AR coated HR-Si lens with OAP mirrors improved the SNR by about 9 dB.

3. While an OAP only setup was also conceived, the results showed that the beam quality focused by an OAP was substantially worse than that from a lens.

4. Although not documented in this work, more rigorous alignment of the beam was achieved by tracking the optical axis using pinhole alignment. This also included optimization of the path lengths between each optical element. Because the imaging system is not in a purged environment, the atmospheric losses in this frequency range are non-negligible. Redesign of the setup for a shorter optical path led to reduced signal attenuation.

For future work, I propose to modify the single-pixel imaging setup to allow simultaneous measurement of the degree of linear polarization (DoLP). This can be made possible with a couple adjustments to the setup presented in this work. The DoLP may provide an additional source of contrast for depolarizing media such as materials with surface roughness. Additionally, future work will involve further exploration of the QC metasurface with electrically switchable polarization states as demonstrated in Ref [46]. A QC-VECSEL based upon this metasurface will allow for electrical switching between two near-orthogonal linear polarization states while maintaining the power output and lasing frequency. Modulation speeds will only be limited by the buildup time of the laser oscillation and the RC time constant of the bias circuit. This could allow real-time imaging with a microbolometer camera to be extended to a polarization sensitive one.

While a wave of activity in THz imaging was seen in the past two decades, relatively little work has been done in polarization sensitive THz imaging. The prospects of THz imaging promised by its high transmission through polymers, high absorption in water, and its non-ionizing photon energies have been well demonstrated. The question that has yet to be convincingly answered is whether or not polarimetric sensing provides additional useful information for THz applications. Indeed, this area of research has yet to mature, and there is more work to be done before any conclusive statements to be made.

REFERENCES

[1] B. S. Williams, *Terahertz quantum cascade lasers*. Thesis, Massachusetts Institute of Technology, 2003.

[2] A. J. L. Adam, I. Kašalynas, J. N. Hovenier, T. O. Klaassen, J. R. Gao, E. E. Orlova, B. S. Williams, S. Kumar, Q. Hu, and J. L. Reno, "Beam patterns of terahertz quantum cascade lasers with subwavelength cavity dimensions," *Applied Physics Letters*, vol. 88, no. 15, p. 151105, 2006.

[3] L. Xu, D. Chen, T. Itoh, J. L. Reno, and B. S. Williams, "Focusing metasurface quantum-cascade laser with a near diffraction-limited beam," *Optics Express*, vol. 24, no. 21, pp. 24117–24128, 2016.

[4] N. C. J. v. d. Valk, W. A. M. v. d. Marel, and P. C. M. Planken, "Terahertz polarization imaging," *Optics Letters*, vol. 30, no. 20, pp. 2802–2804, 2005.

[5] G. S. Jenkins, D. C. Schmadel, and H. D. Drew, "Simultaneous measurement of circular dichroism and Faraday rotation at terahertz frequencies utilizing electric field sensitive detection via polarization modulation," *Review of Scientific Instruments*, vol. 81, no. 8, p. 083903, 2010.

[6] J. Dai, J. Zhang, W. Zhang, and D. Grischkowsky, "Terahertz time-domain spectroscopy characterization of the far-infrared absorption and index of refraction of high-resistivity, float-zone silicon," *JOSA B*, vol. 21, no. 7, pp. 1379–1386, 2004.

[7] M. Bass, C. DeCusatis, J. Enoch, V. Lakshminarayanan, G. Li, C. Macdonald, V. Mahajan, and E. Van Stryland, *Handbook of Optics, Third Edition Volume I: Geometrical and Physical Optics, Polarized Light, Components and Instruments*. USA: McGraw-Hill, Inc., 3 ed., 2009.

[8] T. S. Hartwick, D. T. Hodges, D. H. Barker, and F. B. Foote, "Far infrared imagery," *Applied Optics*, vol. 15, no. 8, pp. 1919–1922, 1976.

[9] M. van Exter and D. Grischkowsky, "Characterization of an optoelectronic terahertz beam system," *IEEE Transactions on Microwave Theory and Techniques*, vol. 38, no. 11, pp. 1684–1691, 1990.

[10] D. M. Mittleman, "Twenty years of terahertz imaging [Invited]," *Optics Express*, vol. 26, no. 8, pp. 9417–9431, 2018.

[11] D. L. Hickman, M. I. Smith, K. S. Kim, and H.-J. Choi, "Polarimetric imaging: system architectures and trade-offs," in *Electro-Optical and Infrared Systems: Technology and Applications XV*, vol. 10795, p. 107950B, International Society for Optics and Photonics, 2018.

[12] J. Qi and D. S. Elson, "Mueller polarimetric imaging for surgical and diagnostic applications: a review," *Journal of Biophotonics*, vol. 10, no. 8, pp. 950–982, 2017.

[13] A. Kadambi, V. Taamazyan, B. Shi, and R. Raskar, "Depth Sensing Using Geometrically Constrained Polarization Normals," *International Journal of Computer Vision*, vol. 125, no. 1-3, pp. 34–51, 2017.

[14] B. B. Hu and M. C. Nuss, "Imaging with terahertz waves," *Optics Letters*, vol. 20, no. 16, pp. 1716–1718, 1995.

[15] B. Williams, S. Kumar, Q. Hu, and J. Reno, "High-power terahertz quantum-cascade lasers," *Electronics Letters*, vol. 42, no. 2, pp. 89–91, 2006.

[16] L. Li, L. Chen, J. Zhu, J. Freeman, P. Dean, A. Valavanis, A. Davies, and E. Linfield, "Terahertz quantum cascade lasers with >1 W output powers," *Electronics Letters*, vol. 50, no. 4, pp. 309–311, 2014.

[17] L. Bosco, M. Franckié, G. Scalari, M. Beck, A. Wacker, and J. Faist, "Thermoelectrically cooled THz quantum cascade laser operating up to 210 K," *Applied Physics Letters*, vol. 115, no. 1, p. 010601, 2019.

[18] J. Darmo, V. Tamosiunas, G. Fasching, J. Kröll, K. Unterrainer, M. Beck, M. Giovannini, J. Faist, C. Kremser, and P. Debbage, "Imaging with a Terahertz quantum cascade laser," *Optics Express*, vol. 12, no. 9, pp. 1879–1884, 2004.

[19] E. Pickwell and V. P. Wallace, "Biomedical applications of terahertz technology," *Journal of Physics D: Applied Physics*, vol. 39, no. 17, pp. R301–R310, 2006.

[20] A. W. M. Lee, Q. Qin, S. Kumar, B. S. Williams, Q. Hu, and J. L. Reno, "Real-time terahertz imaging over a standoff distance (>25meters)," *Applied Physics Letters*, vol. 89, no. 14, p. 141125, 2006.

[21] L. Xu, C. A. Curwen, P. W. C. Hon, Q.-S. Chen, T. Itoh, and B. S. Williams, "Metasurface external cavity laser," *Applied Physics Letters*, vol. 107, no. 22, p. 221105, 2015.

[22] L. Xu, C. A. Curwen, D. Chen, J. L. Reno, T. Itoh, and B. S. Williams, "Terahertz Metasurface Quantum-Cascade VECSELs: Theory and Performance," *IEEE Journal of Selected Topics in Quantum Electronics*, vol. 23, no. 6, pp. 1–12, 2017.

[23] A. J. Fitzgerald, B. E. Cole, and P. F. Taday, "Nondestructive Analysis of Tablet Coating Thicknesses Using Terahertz Pulsed Imaging," *Journal of Pharmaceutical Sciences*, vol. 94, no. 1, pp. 177–183, 2005.

[24] T. Yasui, T. Yasuda, K.-i. Sawanaka, and T. Araki, "Terahertz paintmeter for noncontact monitoring of thickness and drying progress in paint film," *Applied Optics*, vol. 44, no. 32, pp. 6849–6856, 2005.

[25] M. Naftaly, N. Vieweg, and A. Deninger, "Industrial Applications of Terahertz Sensing: State of Play," *Sensors*, vol. 19, no. 19, p. 4203, 2019.

[26] A. W. Lee, T.-Y. Kao, I. A. Zimmerman, N. Oda, and Q. Hu, "Terahertz imaging with quantum cascade lasers," in *Image Sensing Technologies: Materials, Devices, Systems, and Applications III*, vol. 9854, p. 98540R, International Society for Optics and Photonics, 2016.

[27] R. Zhang, Y. Cui, W. Sun, and Y. Zhang, "Polarization information for terahertz imaging," *Applied Optics*, vol. 47, no. 34, pp. 6422–6427, 2008.

[28] K. Xu, E. Bayati, K. Oguchi, S. Watanabe, D. P. Winebrenner, and M. H. Arbab, "Terahertz time-domain polarimetry (THz-TDP) based on the spinning E-O sampling technique: determination of precision and calibration," *Optics Express*, vol. 28, no. 9, pp. 13482–13496, 2020.

[29] Y. Sakai, I. Kawayama, H. Nakanishi, and M. Tonouchi, "Polarization imaging of imperfect m-plane GaN surfaces," *APL Photonics*, vol. 2, no. 4, p. 041304, 2017.

[30] L. Xu, C. A. Curwen, J. L. Reno, and B. S. Williams, "High performance terahertz metasurface quantum-cascade VECSEL with an intra-cryostat cavity," *Applied Physics Letters*, vol. 111, no. 10, p. 101101, 2017.

[31] A. E. Siegman, "How to (Maybe) Measure Laser Beam Quality," in *DPSS (Diode Pumped Solid State) Lasers: Applications and Issues (1998), paper MQ1*, p. MQ1, Optical Society of America, 1998.

[32] "International Organization for Standardization, document no. ISO 11146, Lasers and laser-related equipment – Test methods for laser beam parameters – Beam width, divergence, angle and beam propagation factor," 1999.

[33] T. F. Johnston, "Beam propagation (M^2) measurement made as easy as it gets: the four-cuts method," *Applied Optics*, vol. 37, no. 21, pp. 4840–4850, 1998.

[34] M. Neshat and N. P. Armitage, "Improved measurement of polarization state in terahertz polarization spectroscopy," *Optics Letters*, vol. 37, no. 11, pp. 1811–1813, 2012.

[35] N. A. Rubin, G. D'Aversa, P. Chevalier, Z. Shi, W. T. Chen, and F. Capasso, "Matrix Fourier optics enables a compact full-Stokes polarization camera," *Science*, vol. 365, no. 6448, 2019.

[36] S. Trippe, "Polarization and Polarimetry: A Review," *arXiv:1401.1911 [astro-ph]*, 2014.

[37] S.-X. Huang, Y.-S. Zeng, G.-B. Wu, K.-F. Chan, B.-J. Chen, M.-Y. Xia, S.-W. Qu, and C. H. Chan, "Terahertz Mueller Matrix Polarimetry and Polar Decomposition," *IEEE Transactions on Terahertz Science and Technology*, vol. 10, no. 1, pp. 74–84, 2020.

[38] S. Sung, J. Garritano, N. Bajwa, B. Nowroozi, W. Grundfest, and Z. Taylor, "Analysis and optimization of THz imaging optics with off-axis parabolic mirrors," in *2014 39th International Conference on Infrared, Millimeter, and Terahertz waves (IRMMW-THz)*, pp. 1–2, 2014.

[39] M. Naftaly and R. Dudley, "Terahertz reflectivities of metal-coated mirrors," *Applied Optics*, vol. 50, no. 19, pp. 3201–3204, 2011.

[40] M. Ji, C. Musante, S. Yngvesson, A. Gatesman, and J. Waldman, "Study of Parylene as Antireflection Coating for Silicon Optics at THz Frequencies," 2000.

[41] A. Gatesman, J. Waldman, M. Ji, C. Musante, and S. Yagvesson, "An anti-reflection coating for silicon optics at terahertz frequencies," *IEEE Microwave and Guided Wave Letters*, vol. 10, no. 7, pp. 264–266, 2000.

[42] J. T. Verdeyen, *Laser electronics / Joseph T. Verdeyen.* Prentice-Hall Englewood Cliffs, N.J, 1981.

[43] A. Podzorov and G. Gallot, "Low-loss polymers for terahertz applications," *Applied Optics*, vol. 47, no. 18, pp. 3254–3257, 2008.

[44] S. Priebe, M. Jacob, and T. Kürner, "Polarization investigation of rough surface scattering for THz propagation modeling," in *Proceedings of the 5th European Conference on Antennas and Propagation (EUCAP)*, pp. 24–28, 2011.

[45] N. Vieweg, F. Rettich, A. Deninger, H. Roehle, R. Dietz, T. Göbel, and M. Schell, "Terahertz-time domain spectrometer with 90 dB peak dynamic range," *Journal of Infrared, Millimeter, and Terahertz Waves*, vol. 35, no. 10, pp. 823–832, 2014.

[46] L. Xu, D. Chen, C. A. Curwen, M. Memarian, J. L. Reno, T. Itoh, and B. S. Williams, "Metasurface quantum-cascade laser with electrically switchable polarization," *Optica*, vol. 4, no. 4, pp. 468–475, 2017.